Rational Functions and Other Techniques for RF and Microwave Modeling

Arash Kashi

A Thesis

in

The Department

of

Electrical and Computer Engineering

Presented in Partial Fulfillment of the Requirements

for the Degree of Master of Applied Science (Electrical and Computer Engineering) at

Concordia University

Montréal, Québec, Canada

September 2007

Your file Votre référence
ISBN: 978-0-494-34699-0
Our file Notre référence
ISBN: 978-0-494-34699-0

ABSTRACT

Rational Functions and Other Techniques for RF and Microwave Modeling

Arash Kashi

This thesis contributes several techniques for electromagnetic-based computer-aided modeling of microwave components exploiting rational functions, space mapping, Finite Difference Time-Domain (FDTD) method etc.

First, enhanced adaptive sampling algorithms, both in single and multi-dimensions, are proposed. The algorithms are based on rational interpolation, which leads to more accurate high-frequency models as compared to other existing interpolants, *e.g.* spline. Starting with a minimal number of support points, *i.e.* electromagnetic data, and with lowest-order rational functions, the algorithms systematically produce models, which meet user-specified accuracies. In each stage of these algorithms new support points are adaptively selected based on model errors. The advantages of the proposed algorithms are shown through practical RF and microwave examples.

Second, a new space-mapping based CAD methodology for modeling temperature characteristics of combline resonators is proposed. With the aid of two commercial simulation tools, namely Ansoft's *HFSS* and Agilent's *ADS*, this methodology generates accurate temperature models of combline resonators. The method is generic *i.e.* it is capable of generating corresponding models for a variety of resonator structures including the mushroom and straight. The model generated using space mapping is suitable for compensation methods where the type of material to be used has yet to be determined.

Third, a FDTD based technique, integrated with rational functions has been developed to generate fast and accurate temperature models for combline resonators. Through examples, it has been shown that a FDTD algorithm with 2D uniform-grid distribution is fully capable of modeling temperature behavior of combline resonators.

The advantage of this work over other numerical solutions in terms of computational complicity and required simulation time is illustrated. This technique can be applied to compensation methods requiring geometry optimization.

To my parents
Seddigheh and Ali

Acknowledgements

I wish to express my sincere appreciation to my supervisor Dr. Vijay Devabhaktuni for his expert supervision, continuing encouragement and constant support during the course of this work.

I also wish to acknowledge Mr. Pavan Kumar (former senior RF/microwave engineer of Mitec currently with COM DEV) and Mr. Martin Caron (senior RF/microwave engineer), my managers in Mitec Telecom Inc., for their constant support throughout summer 2006.

I would also like to express my sincere appreciation to PHD students, Amir Hajiaboli and Alper Ozturk, and Dr. Don Davis, for their precious advice on chapter 4 of the thesis.

I would like to extend my thanks to my colleagues Kaustubha Mendhurwar, Amir Hossein Yamini, Li Zhu, Niladri Roy and Navid Arbabi for their suggestions and support in preparing this manuscript.

Finally, I would like to express my deep gratitude to my parents, Seddigheh and Ali, who gave me the strength to finish this work, for their continued care and support.

Contents

List of Figures

List of Tables

List of Symbols

$\boldsymbol{y}$	EM responses in the form of scattering parameters
f	Frequency
$\boldsymbol{x}$	Vector of geometrical designable parameters
$\boldsymbol{x}_{new}$	Designable parameters at a new plan
x_{ref}	Designable parameters at a reference plan
$\boldsymbol{p}$	Vector of geometrical designable parameters and frequency
$S^{u,v}$	Rational interpolant of degree u and v in numerator and denominator
a_i, b_j	Unknown coefficients of the rational function $S^{u,v}$
u	Degree of the numerator in a rational interpolant
v	Degree of the denominator in a rational interpolant
S_n	Rational interpolant of order n
$\boldsymbol{B}$	Vector containing unknown coefficients of $S^{u,v}$
$\boldsymbol{A}$	Matrix of linear set of equations for unknown coefficients of $S^{u,v}$
$\boldsymbol{L}$	Left displacement operator
$\boldsymbol{R}$	Right displacement operator
α	Displacement rank
$\hat{\boldsymbol{A}}$	Displacement ranked of matrix $\boldsymbol{A}$
T_i	Chebyshev polynomial of order i
L_i	Legendre polynomials of order i
δ_k	Residual function in the k^{th} stage
Δ_k	Dynamic grid size in the k^{th} stage

E_k	Termination criterion in the k^{th} stage
E_d	Desired accuracy
f^*	Adaptively located frequency
f_g	Potential frequency location on the dynamic grid
ϵ	Distance between the rational models of different order
ϕ	Solutions of a homogenous linear system
I_s	Frequency range of interest
Γ	A fine set of grid points along frequency
Σ	Set of training EM samples
Ω	Set of potential EM samples
$\Lambda_{k,l}$	Distance of $S^{k,l}$ from the the other current interpolants
M	Total possible pole-zero arrangements for the rational interpolant
$\phi_{k,l}$	Dispersion between the short-listed rational interpolants
ζ	User-specified accuracy in the proposed 1D algorithm B
η, ξ	Degrees corresponding to the Taylor mapping
N	Number of short-listed least dispersed interpolants
γ_i, ρ_i	Unknown coefficients of the Taylor mapping
C_{gap}	Gap capacitance
C_{screw}	Screw capacitance
$C_{fringing}$	Fringing capacitance
C_e	Effective capacitance
θ	Electrical length
Z_0	Characteristic impedance
$\boldsymbol{x}_c$	Vector of coarse model parameters
$\boldsymbol{x}_{exp}$	Expanded designable values
$\boldsymbol{x}_c^*$	Vector of optimal coarse model parameters
$\boldsymbol{x}_f$	Vector of fine model parameters

$\boldsymbol{R}_c$	Vector of optimal coarse model responses
$\boldsymbol{R}_s$	Vector of optimal surrogate model responses
$\boldsymbol{R}_f$	Vector of optimal fine model responses
$\boldsymbol{P}^{(i)}$	Mapping $\boldsymbol{P}$ in the i^{th} iteration
m	Number of frequency points
$ratio, offset$	Mapping coefficients
k_c	Compensation coefficient for FDTD dispersion
t_c	Centre time for BH excitation
N_{half}	Duty cycle of the Gaussian excitation in seconds
C_n, ω_n	Unknown coefficients of Padé approximation
k_d	Convergence criterion

Chapter 1

Introduction

1.1 Motivation

Computer aided design (CAD), often referred to as design automation, has progressed considerably in recent years owing to R&D contributions both in the form of approximate models and full-wave simulators. Currently, there is a strong demand from industry for accurate CAD tools that allow first-pass design of radio-frequency (RF) and microwave modules. This first-pass design is becoming possible with the aid of optimization techniques that emerged during the past three decades [1][2]. These techniques have provided designers with strong and reliable CAD tools necessary for complex and demanding needs of modern circuit design.

As operating frequency increases, EM effects become more critical. Recently, commercial software packages Such as Sonnet software [3] and Ansoft's *HFSS* have been developed to fully account for high order EM effects in modern circuit design. Such simulators are denoted as Electromagnetic (EM) simulators and the solutions provided by these simulators are denoted as "fine" solutions. EM simulators exploit different numerical methods. For example Ansoft's *HFSS* is based on Finite Element (FEM) and Agilent's *ADS* is based on Method of Moments (MoM). However, high computational resources are required for large and complex microwave structures,

especially for CAD operations such as Monte-Carlo analysis, yield optimization, and so forth.

One typical way engineers have tried to incorporate basic EM effects is to use knowledge-based models. For instance, several empirical and circuit models of many microwave circuits have been developed and used frequently. The empirical and circuit-theoretic models are denoted as "coarse" models. Circuit models may be considered to alleviate RF/microwave design problems, because they are computationally efficient. However, circuit models for multi-port devices are difficult to construct and their accuracy over a wide band is questionable.

In the light of above discussion, research on EM-based fast models that are reliable at high frequencies and account for high order EM effects is becoming important. Recent approaches in this direction include look-up tables [5], interpolation techniques [6], space mapping (SM) [7] and artificial neural networks (ANN) [8]. Look-up tables are built from exhaustive execution of EM simulation. These exhaustive simulations become prohibitively large in case of large number of design parameters and multi-port components. Interpolation techniques can be used to extract a fine response using limited number of data. Interpolation models can be quickly evaluated, and hence are well-suited for circuit optimization and statistical design [9]. Among interpolation techniques, rational functions are best-suited for interpolation of scattering parameters of microwave components. Rational interpolants yield accurate EM approximations owning to their pole-zero arrangement, in cases where other traditional interpolants, *e.g.* polynomial functions, fail. In situations where both coarse and fine models of a passive component are available, space mapping is efficient. Space Mapping combines the computational efficiency of empirical/circuit-theoretic models with the accuracy of the EM simulator. A mathematical link (mapping) is established between the spaces of the parameters of the empirical and EM models. This approach directs the bulk of the required CPU time to the fast model while preserving the accuracy and confidence supplied by few EM analyses. ANN modules have

recently gained attention as an useful tool for RF and microwave modeling. ANNs are first trained offline to learn high-frequency component behaviors from EM data. The resulting neural models are then used to facilitate efficient EM based CAD of RF/microwave circuits.

In spite of these advances, EM-based modeling remains an open research topic. In this thesis, several EM-based modeling techniques combining a variety of above-mentioned techniques are researched upon.

1.2 Objectives

- Reducing the number of EM data required for accurate EM-based frequency modeling techniques up to 40% through the use of rational functions.
- Developing improved multidimensional modeling algorithms for general cases where there is no distinguishable highly non-linear design parameter while reducing the number of required EM samples up to 10% in comparison to standard algorithms.
- Formulating improved multidimensional modeling algorithms for special cases where the model-input space can be divided into two sub-spaces namely highly non-linear and relatively less non-linear while reducing the number of required EM samples up to 25% in comparison to standard algorithms through the use of rational functions together with a hybrid mapping.
- Exploring temperature models for combline resonators with accuracies in terms of cut-off frequency drift as impressive as $+2ppm/°C$ through the use of space mapping and FDTD.

1.3 Thesis Outline

The thesis discusses different modeling techniques applicable to RF and microwave design and optimization. Since these techniques are based on different mathematical tools and serve different applications, literature review related to each technique is included in the corresponding chapter.

Chapter 2 introduces rational functions as an interpolation tool in modeling of RF/microwave components. The importance of adaptive sampling in RF/microwave modeling is explained and the standard algorithm based on rational functions is reviewed. The new concept of dynamic grid is proposed and is integrated into the standard adaptive sampling algorithm. The enhancements as a result of the dynamic grid application are illustrated through practical examples. It has also shown that in severely non-linear cases, conventional multidimensional modeling algorithms fail and hence a new multidimensional modeling algorithm is presented that facilitates design/optimization of RF/microwave components.

Chapter 3 presents space mapping as a tool to modeling temperature behavior of cylindrical resonators. A review of conventional temperature modeling of combline resonators is presented. The concept of space mapping is reviewed and a space mapping temperature modeling framework is fully explained in both Ansoft's *HFSS* and Agilent's *ADS*. The accuracy of this technique is validated through a comparison with measurement results.

In Chapter 4, the application of FDTD method for temperature modeling of combline resonators is proposed. A simplified FDTD method is integrated with Padé approximation to generate a fast and accurate temperature model for combline resonators of arbitrary structure. It has been shown that a simplified finite difference method with 2D uniform-grid distribution is fully capable of modeling the temperature behavior of combline resonators.

1.4 Contributions

The author contributed to the following original developments:

- A new dynamic grid concept is developed and incorporated into single and multi dimensional modeling algorithms based on rational interpolants.
- A new multi dimensional RF/microwave modeling algorithm combining rational interpolants, hybrid mapping and genetic concepts is proposed.
- A framework for temperature modeling of combline resonators (cylindrical cavity resonators), exploiting space mapping concept, is proposed.
- Application of FDTD method incorporated with Padé approximation is proposed for temperature modeling of combline resonators.

Chapter 2

RF/Microwave Modeling Algorithms Based on Adaptive Sampling

2.1 Introduction

Novel approaches for development of EM-based models from EM data leading to accurate/fast CAD of RF/microwave circuits are constantly evolving. One of the techniques gaining attention is neural networks. Neural networks are trained offline to learn RF/microwave component behaviors from EM data. Resulting neural models are used to facilitate efficient CAD of RF/microwave circuits [10]. In situations where both coarse and fine models of a passive component are available, space mapping [7] is a preferred modeling approach.

Here, the challenges in EM-based modeling are reviewed from different perspectives. In general, acquisition of EM data through full-wave simulations tends to be computationally intensive. This motivates research on algorithms that facilitate development of accurate and fast EM-based models using as little EM data as possible. Latest research in this direction includes knowledge based neural networks [11], trust-

region aggressive space mapping [12], etc.

Here, the challenges in EM modeling from the perspective of EM data generation, which is a key prerequisite to RF/microwave modeling, are discussed. The task of data generation involves important decisions with regard to the distribution of sampling locations in the EM design parameter space. One common practice is to employ "equidistant sampling", which is also referred to as "uniform distribution". In order to achieve the desired model accuracy in highly nonlinear regions, such an approach often necessitates a fine sampling grid. In the case of highly complicated EM structures, which operate at higher and higher GHz frequencies, uniform sampling demands even finer grids, thereby making it computationally prohibitive and impractical [13]. In essence, there is a need for novel sampling strategies.

Latest research in EM-based modeling revolves around the application of adaptive sampling algorithms. Examples include adaptive frequency sampling algorithms based on polynomials [14] and rational interpolants [15][16], as well as novel concepts such as error-based sampling [17] and automatic model generation [18]. For instance, a rational function model of a microstrip filter was presented in [19]. Interestingly, this chapter incorporates both "efficient modeling" and "efficient sampling" approaches in advanced research.

In a recent work [16], adaptive sampling algorithms based on a dynamic grid is presented in single dimension. These algorithms have been shown to outperform a standard algorithm [15] in terms of convergence and model accuracy.

This chapter describes a detailed framework of enhanced adaptive sampling algorithms A and B as applied to rational interpolants both in single and multidimensional problems. Starting with a minimal number of EM data and with lowest-order rational functions, these algorithms automatically proceed in a stage-wise manner. After each stage, the model error is compared with the user-specified accuracy to decide whether to terminate the algorithm(s) or to proceed to the next stage. Appropriate error measures are used for both adaptive sampling and model validation. Due to

their iterative nature, the number of EM data used to build satisfactory models is kept as low as possible. The performance of the proposed algorithms is compared with standard algorithms through practical RF/microwave examples.

2.2 Rational Functions

Let $\boldsymbol{x}$ represent a vector containing physical parameters of an RF/microwave component not including frequency (f), and $\boldsymbol{y}$ represent a vector containing its EM responses. The EM relationship between $\boldsymbol{x}$ and $\boldsymbol{y}$ can be expressed as

$$\boldsymbol{y} = \boldsymbol{g}_{EM}(\boldsymbol{x}, f). \tag{2.1}$$

In the EM-CAD area, $\boldsymbol{g}_{EM}$ is available to designers in the form of commercial simulators. At microwave frequencies, $\boldsymbol{g}_{EM}$ tends to be highly nonlinear with respect to both $\boldsymbol{x}$ and f. In general, the objective of EM based modeling algorithms is to develop a fast and accurate surrogate model $\boldsymbol{g}$ based on EM data from $\boldsymbol{g}_{EM}$. The EM data, *i.e.* $(\boldsymbol{x}_i, f_i, \boldsymbol{y}_i)$, where i is the sample index, are obtained *via* repetitive execution of an EM simulator. In the 1D case, $\boldsymbol{x}$ is kept constant and f alone is sampled. As such, EM data used are of the form (f_i, y_i). Once all or part of the EM data is acquired from simulations, an appropriate input-output mapping function needs to be identified to proceed with model development. In practice, an interpolation function that can take into account the physics behind the problem becomes a natural choice.

In the last decade, several researchers have demonstrated both univariable [21][22][23] and multivariable [15][19][24] interpolation functions. Among them, a popular RF/microwave oriented interpolant is the rational function. Rational functions are best-suited for interpolation of scattering parameters (S-parameters) of microwave components. For example, rational interpolants such as (2.2) yield accurate EM approximations owing to their pole-zero arrangement, in situations where other traditional interpolants, *e.g.*

polynomial functions, fail. A general-form of a rational function is given by

$$S^{u,v} = \frac{a_0 + a_1 f + \cdots + a_u f^u}{1 + b_1 + \cdots + b_v f^v}, \tag{2.2}$$

where a_k and b_l are unknowns. To determine these coefficients, at least $1 + u + v$ EM data points are required. The order of a rational function can be defined as the number of EM data used to solve for a_k and b_l. Let S_n represent an n^{th}-order rational function *i.e.* $n = u + v + 1$. Rational functions of the same order can have different pole-zero arrangements (*i.e.* different combinations of u and v) and as to which of the arrangments better suits an EM modeling problem is not known *a priori.*

There are several classic algorithms to generate a rational model. All these techniques can be classified into two groups. In the first group, $S^{u,v}$ is determined for an arbitrary f without solving for unknown coefficients *i.e.* a_k and b_l. Examples of such indirect algorithms are Neville-type, where $S^{u,v}$ is indirectly evaluated through an iterative process. In the second group, the unknown coefficients of $S^{u,v}$ are directly determined. Once the coefficients are determined, the realized rational function can replace the physical model. Examples of direct algorithms are Gaussian elimination, Gauss-Jordan algorithms and Choleski decomposition algorithms [27]. Two following sections are overviews of the commonly used algorithms *i.e.* Neville-type and Gaussian elimination.

2.3 Neville-Type Algorithms

In order to determine the value of interpolating rational function for a single value of f, a Neville-type algorithm [27], proven to be fast and stable for lower order rational functions, is given by

$$S^{i,j}(f) = S^{i,j-1}(f) + \frac{S^{i,j-1}(f) - S^{i-1,j-1}(f)}{\frac{f-f_{i,j}}{f-f_i}\left[1 - \frac{S^{i,j-1}(f) - S^{i-1,j-1}(f)}{S^{i,j-1}(f) - S^{i-1,j-2}(f)}\right] - 1}, \tag{2.3}$$

where i is the index of n EM data, j is the iteration number, and $1 \leq j < n$.

Recursive Neville-type algorithms are useful only if the function value of the desired interpolant is required at a small number of points different from the support points. However, in adaptive sampling algorithms, the rational interpolant needs to be evaluated over an entire high-dimension grid in order to approximate the error function and locate new sampling points. Hence, Neville type algorithms are not efficient solutions for afore-metioned problems. Alternatively, direct algorithms such as Gaussian elimination and Gauss-Jordan, which compute the coefficients of the rational model and lead to an explicit representation of rational model, are more efficient for the fast computation of rational model over a fine grid of data.

2.4 Gaussian Elimination

Gaussian elimination is a method for solving a linear set of equations. In the context of the previous formulation, the set of equations will be of form of

$$\boldsymbol{A}\boldsymbol{B} = \boldsymbol{y}, \tag{2.4}$$

where

$$\boldsymbol{A}_{(1+u+v)\times(1+u+v)} = \begin{bmatrix} 1 & f_1 & \cdots & f_1^u & -y_1 f_1 & -y_1 f_1^2 & \cdots & -y_1 f_1^v \\ 1 & f_2 & \cdots & f_2^u & -y_2 f_2 & -y_2 f_2^2 & \cdots & -y_2 f_2^v \\ \vdots & \vdots & \vdots & \vdots & \vdots & \vdots & \vdots & \vdots \\ 1 & f_n & \cdots & f_n^u & -y_n f_n & -y_n f_n^2 & \cdots & -y_n f_n^v \end{bmatrix},$$

$$\boldsymbol{B}_{(1+u+v)\times 1} = \begin{bmatrix} a_0 \\ \vdots \\ a_u \\ b_1 \\ \vdots \\ b_v \end{bmatrix},$$

and

$$\boldsymbol{y}_{(1+u+v)\times 1} = \begin{bmatrix} y_1 \\ \vdots \\ \vdots \\ \vdots \\ \vdots \\ y_n \end{bmatrix}, \tag{2.5}$$

where n represents the number of support points or samples. After converting (2.4) into an augmented form, elementary row operations are carried out to generate an upper triangle matrix. The equation of the $(1+u+v)^{th}$ row is solved for b_v which is then substituted back into the equation of the $(u+v)^{th}$ row to obtain a solution for b_{v-1}. This iterative process is continued until all the unknown coefficients are determined.

Critical aspects of Gaussian elimination, *i.e.* computational complexity and matrix conditioning, are already addressed in literature. An overview of technical details is presented in the following subsections.

2.4.1 Displacement Rank

A standard Gaussian elimination scheme performs $O(n^3)$ operations. Converting the Gaussian elimination procedure into appropriate operations such as displacement rank structure results in fast $O(n^2)$ algorithms which allows faster triangular factorization

of a matrix [29].

According to [29] the displacement rank α of an $(1+u+v) \times (1+u+v)$ matrix $\boldsymbol{A}$ is defined as the rank of the matrix $\boldsymbol{LA} - \boldsymbol{AR}$ with $\boldsymbol{L}$ and $\boldsymbol{R}$ being the so-called left and right displacement operators. If $\boldsymbol{A}$ is a Vandermonde matrix (common form of matrix generated for solving the unknown coefficients of rational functions), then the suitable displacement operators are given by

$$\begin{aligned} L &= diag(1/y_0, \ldots, 1/y_{1+u+v}) \\ R^T &= Z_u^{(1)} \oplus Z_{v+1}^{(1)}, \end{aligned} \tag{2.6}$$

with

$$Z_k^{(\omega)} = \begin{bmatrix} 0 & \cdots & \cdots & 0 & \omega \\ 1 & 0 & \cdots & \cdots & 0 \\ 0 & 1 & \ddots & & \vdots \\ \vdots & \cdots & 0 & 1 & 0 \end{bmatrix}_{k \times k}. \tag{2.7}$$

The resulting matrix $\boldsymbol{LA} - \boldsymbol{AR}$ then takes the form

$$\boldsymbol{LA} - \boldsymbol{AR} = \tag{2.8}$$

$$\begin{bmatrix} y_0(1-x_0^v) & 0 & \cdots & 0 & -(1/x_0 - x_0^u) & 0 & \cdots & 0 \\ \vdots & \vdots & \vdots & \vdots & \vdots & \vdots & \vdots & \vdots \\ y_{1+u+v}(1-x_{1+u+v}^v) & 0 & \cdots & 0 & -(1/x_{1+u+v} - x_{1+u+v}^u) & 0 & \cdots & 0 \end{bmatrix}_{k \times k}. \tag{2.9}$$

Hence, the displacement rank α of $\boldsymbol{A}$ equals $\alpha = 2$. From a factorization

$$LA - AR = GB, \qquad G \in \mathbb{C}^{(1+u+v)\times\alpha}, \; B \in \mathbb{C}^{\alpha\times(1+u+v)}. \tag{2.10}$$

An LU factorization of the Cauchy matrix $\hat{A} = A(Q_{1,v}^H \oplus Q_{1,u+1}^H)$ can be obtained from [29] with order of complexity $O((1+u+v)^2)$. Here the subscript ^{H} denotes complex conjugation and transposition, and the columns of the matrices $Q_{1,v}$ and

Table 2.1: Comparison of conditioning in different bases for example of section 2.10.3

Dim(A)	f_i	$T_i(f)$	$L_i(f)$
18	5.6×10^5	5.6×10^3	5.7×10^3
20	7.5×10^5	7.5×10^3	7.4×10^3
22	6.6×10^6	6.6×10^4	6.3×10^4
24	1.2×10^8	9.8×10^4	9.0×10^4

$Q_{1,u+1}$ contain the eigenvectors of R^T. By exploiting the displacement structure of the matrix $\boldsymbol{A}$, the complexity of solution computation is thus reduced from $O((1+u+v)^3)$ to $O((1+u+v)^2)$.

2.4.2 Orthogonal Basis

Condition number associated with a problem is a measure of that problem's amenability to digital computation, that is, how numerically well-posed the problem is. A problem with a low condition number is said to be well-conditioned, while a problem with a high condition number is said to be ill-conditioned.

Linear set of equations in solving rational functions coefficients are usually ill-conditioned matrices and hence the determined coefficients are sensitive to the perturbation of matrix A [28]. As the solution proposed in [28], the multivariable rational data fitting problems are formulated in terms of an orthogonal basis, such as $T_i(f)$ of the Chebyshev polynomials or $L_i(f)$ of the Legendre polynomials, instead of multinomial basis f_i. For the example in section 2.10.3, the condition numbers in different bases are compared in Table 2.1. As it can be seen, the condition numbers, using Chebyshev and Legendre, are highly improved in compare to the ones with monomial bases.

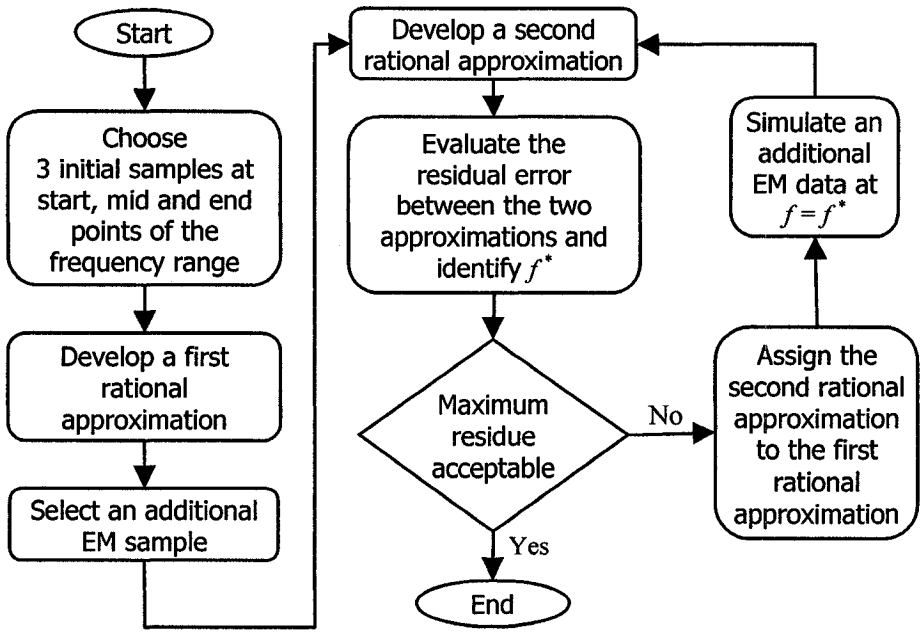

Figure 2.1: Flow-chart of the standard algorithm [15].

2.5 Standard 1D Adaptive Sampling Algorithm

The key to efficient adaptive sampling is minimizing the need for EM data. Choosing a reasonable number of EM data at critical frequencies (*e.g.* resonant frequency of a microstrip filter), at which $\boldsymbol{y}$ is highly nonlinear *w.r.t.* f, becomes critical. Here, an adaptive sampling algorithm [15], used for the purpose of comparison, is briefly reviewed. The standard algorithm shown in Fig. 2.1 begins with two rational functions of orders 3 and 4 respectively. Initial samples are chosen at the two extremities and in the middle of the frequency range of interest $[f_{min}, f_{max}]$. The frequency sample f^* at which new EM data needs to be simulated is given by

$$f^* = \arg\max_f \left\{ \frac{|S_n(f) - S_{n-1}(f)|^2}{1 + |S_n(f)|^2} \right\} \tag{2.11}$$

where $S_n(f)$ and $S_{n-1}(f)$ represent the best and the second best rational approxi-

mations and n represents the number of EM samples that have been used thus far. This ensures that the maximum error of $S_n(f)$ *w.r.t.* $\boldsymbol{g}_{EM}$ is minimized in $S_{n+1}(f)$.

The results are promising, especially in situations where EM responses are relatively smooth. In cases where the frequency response of a component exhibits sudden variations or spikes, this algorithm could either miss such variations entirely or could get trapped in the vicinity of one of many such spikes. Such a phenomenon is undesirable, since further increasing the number of EM samples would not improve the rational model accuracy. Consequently, the total number of EM data points used by this algorithm could exceed that required by a crude non-adaptive sampling algorithm for a given user-specified model accuracy.

2.6 Proposed 1D Adaptive Sampling Algorithm A

The standard algorithm [15] reviewed in section 2.5 determines the new frequency sample based on an l_2-error measure and uses the same measure to check for the termination condition. In automated CAD tools, it is important that any such measures used be obvious to users and hence can be user-inputs to the algorithm. Motivated by [10], a residual function at the end of the k^{th} stage is formulated in l_1-sense as

$$\delta_k(f) = \frac{|S_{k+2}(f) - S_{k+1}(f)|}{\max\{S_{k+2}(f)\} - \min\{S_{k+2}(f)\}}, \tag{2.12}$$

Based on (2.12), frequency f^* at which new data needs to be simulated is given by

$$f^* = \arg\max_f \{\delta_k(f)\}. \tag{2.13}$$

At this juncture, an important aspect of the proposed algorithm A is discussed. The standard algorithm, which allows frequency sampling at any numerical value $f \in [f_{min}, f_{max}]$, has been observed at times to get trapped in certain frequency neighborhoods. On the other hand, it has been noted that crude non-adaptive sampling

algorithms based on a uniform-grid yield highly accurate models, when a sufficiently fine grid is permitted. Motivated by these observations, a new dynamic (*i.e.* pre-defined and iteratively readjusted) grid is presented, which tends to be "adaptive" globally and "grid-based" locally. As a result, in the proposed algorithm A, a new data point is generated not necessarily at f^* but at some f_g, where f_g is an allowed grid point in the neighborhood of f^*.

Since the proposed algorithm operates in a stage-wise manner, it is important to define a termination criterion, *i.e.*

$$E_k = \frac{1}{L}\left(\sum_{i=1}^{L} |\delta_k(f_i)|\right), \tag{2.14}$$

where L is the total number of frequencies at which the residual function in (2.12) is evaluated. In practice, L is allowed to be very large, since rational function evaluations are computationally inexpensive. A systematic framework of the algorithm is shown in Fig. 2.2 and the pseudocode is presented below.

Let user-input $[f_{min}, f_{max}]$ represent the frequency interval of interest. User inputs also include initial number of subintervals 2^m and desired model accuracy E_d.

Initialization: Set $k = 1$. Initial grid-size is calculated as

$$\Delta_k = \frac{f_{max} - f_{min}}{2^m}. \tag{2.15}$$

Using the above grid definition, the algorithm creates 2^{m+1} possible frequency sampling locations or grids.

Stage 1: Two EM data are simulated at f_{min} and f_{max} using an EM solver. Based on these samples, a second-order rational approximation S_2 is developed. An additional EM data is generated at f_{mid}, *i.e.* the mid-point of $[f_{min}, f_{max}]$. Based on the three samples, a third-order rational approximation S_3 is developed. Residual function $\delta_{k=1}(f)$ at the end of the first stage is computed using a fine-grid. Error E_1

is calculated using $\delta_{k=1}(f)$. If $E_1 > E_d$, then set $k = k + 1$, otherwise STOP.

Stage k: Set $\Delta_k = \Delta_{k-1}$. Frequency f^* around which a new EM data point needs to be simulated is identified using (2.13). In the array of possible sample locations, unused grid frequency f_g closest to f^* is located. If $|f^* - f_g| >> \Delta_k$, then GO TO *RedefineGrid*, otherwise set $f^* = f_g$. Simulate EM data at f^*. Proceed to develop a $(k+2)^{th}$ order approximation. GO TO *CheckTerminationCondition.*

RedefineGrid: Set $m = m+1$, re-evaluate and update the array of possible sample locations. Unused grid frequency f_g closest to f^* is located. If $|f^* - f_g| >> \Delta_k$, then GO TO *RedefineGrid*, otherwise set $f^* = f_g$. RETURN Δ_k and f^*.

CheckTerminationCondition: Residual function $\delta_k(f)$ at the end of the k^{th} stage is computed using a fine-grid, based on which E_k is calculated. If $E_k > E_d$, then set $k = k + 1$ and GO TO stage k, otherwise STOP.

2.7 Proposed 1D Adaptive Sampling Algorithm B

In the proposed algorithm A, the fact that multiple rational functions (*i.e.* with different pole-zero arrangements) exist for a given number of EM samples is not taken into account. This could indirectly slow down the convergence of algorithm A.

The proposed algorithm B performs a trial-and-error with all possible combinations of u and v with regard to the equation (2.2). Consequently, this algorithm is able to choose a relatively better pole/zero arrangement, which in turn allows a relatively better sample selection (*i.e.* f^* or f_g).

2.7.1 Motivation

According to [27], if ϕ_1 and ϕ_2 are both solutions of a homogenous linear system $S^{u,v}$, then ϕ_1 and ϕ_2 are equivalent (*i.e.* $\phi_1 \equiv \phi_2$) and hence determine the same rational function. As such, for a given set of EM data, it may be perceived that there exists a unique rational function with an unknown pole-zero arrangement, which best

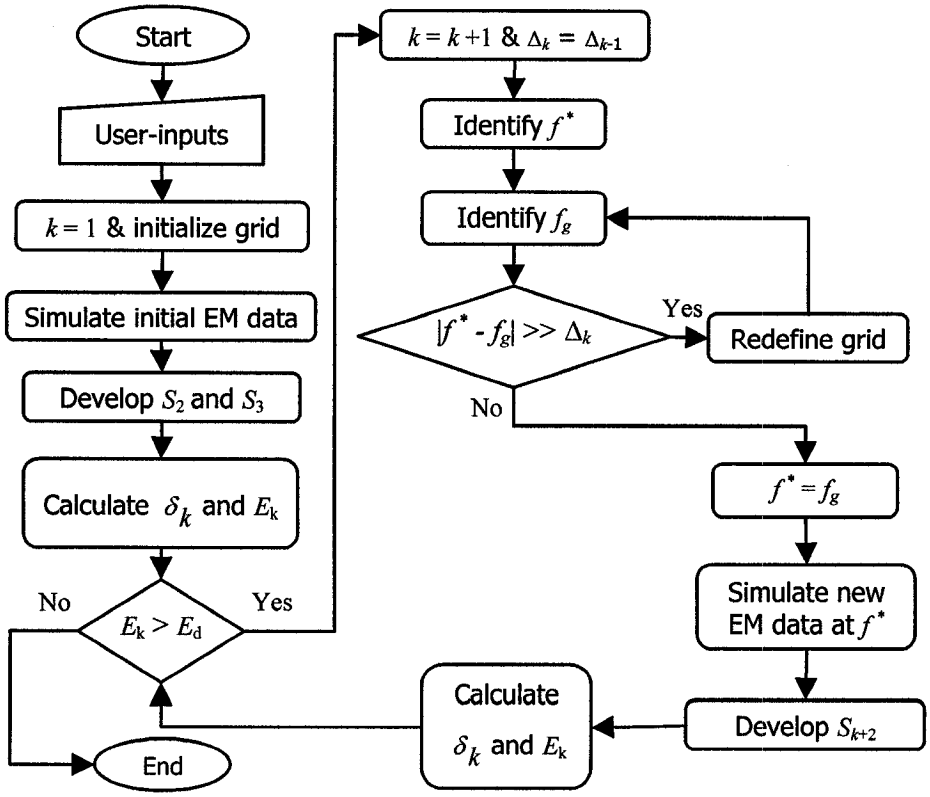

Figure 2.2: Flow-chart of the proposed adaptive sampling Algorithm A from [16].

approximates the EM response. Of course, the problem here is to search for and find that unique rational function.

Consider two rational interpolants, $S^{1,2}(f)$ and $S^{2,1}(f)$, developed using the same set of EM samples ($K = 3$). The distance between them is bounded by ϵ, *i.e.*

$$\left|S^{1,2}(f) - S^{2,1}(f)\right| \leq \epsilon \quad \forall \ f \in I_s. \tag{2.16}$$

Both from literature and from our experimental studies, it has been noted that closely bounded rational interpolants (from among a family of rational interpolants) typically represent a relatively accurate microwave response. Intuitively, it would appear that iteratively selecting "closely bounded" models and using them to identify the next

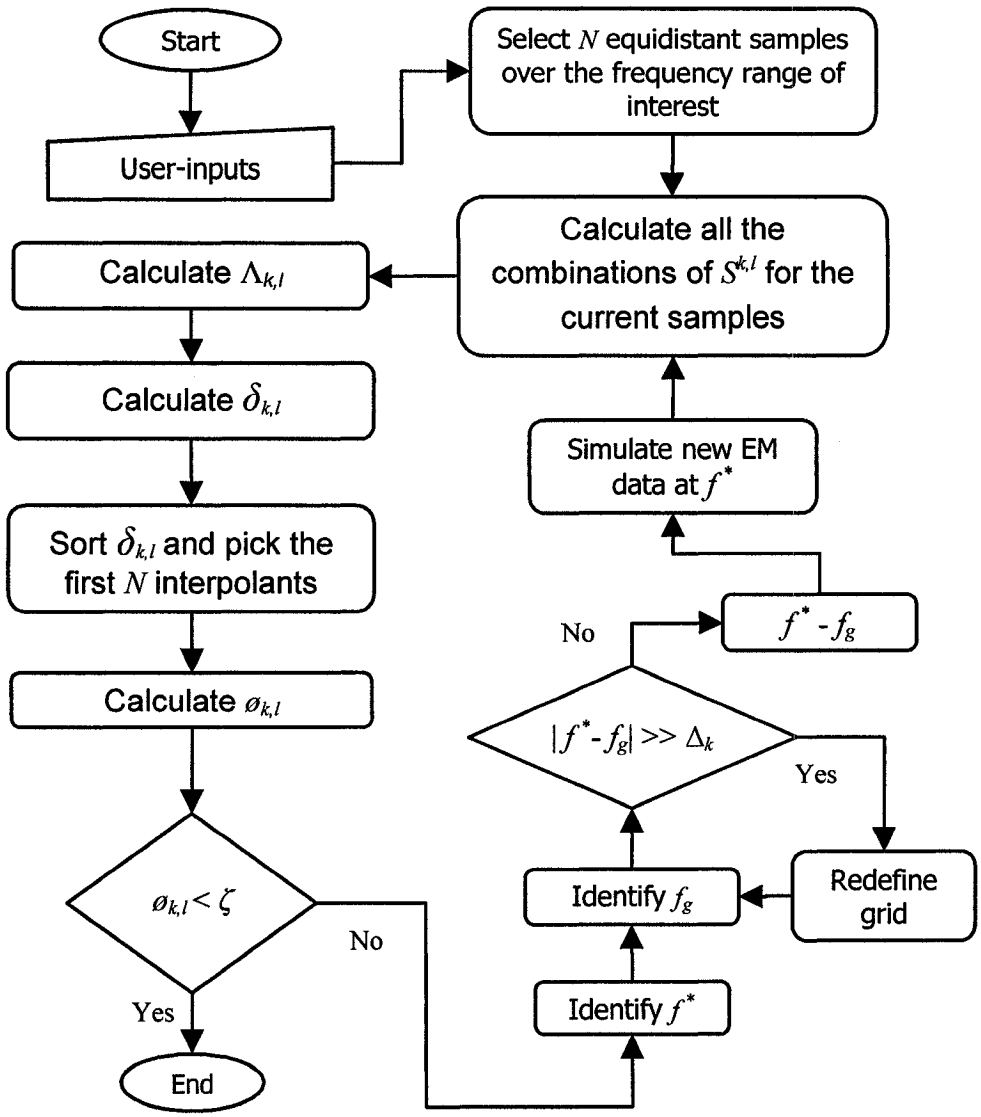

Figure 2.3: Flow-chart of the proposed adaptive sampling algorithm B.

best EM sample could accelerate convergence. Motivated by the above discussions, the proposed algorithm B considers all possible pole-zero arrangements but only picks the closely-bounded interpolants.

2.7.2 Definitions

Let $S^{u,v}(f)$ denote a generalized S-parameter to be modeled in the frequency interval of interest $I_s = [f_{min}, f_{max}]$. Here, u and v represent the degree of the numerator and the denominator respectively. Within this interval of interest, a set $\Gamma = f_i$ consisting of L discrete frequency grid points is defined by the user. Since Γ is primarily used for rational function evaluations and not for EM simulations, these grids can be as fine as possible (*i.e.* L is allowed to be very large). A set Ω, which represents potential EM sampling locations, is defined as $\Omega = f_j \subset \Gamma$. Let $\Sigma \subset \Omega$ represent a set of K EM data given by $\Sigma = \{(f_k, y_k)\}, f_k \in \Omega$. Both Ω and Σ are defined by the user initially and updated by the algorithm iteratively. Conceptually, the algorithm converges when Σ is able to provide adequate EM samples in all critical sub-regions of the design-parameter space.

2.7.3 Implementation

The algorithm begins with $K = N$ user-defined EM data. Here, N also denotes the initial number of rational interpolants involved in calculating the next EM sampling location. The algorithm evaluates unknown coefficients corresponding to all possible rational interpolants (*i.e.* with different pole-zero arrangements). For example, if the algorithm begins with three EM data points, coefficients of three rational models $S^{2,0}$, $S^{1,1}$ and $S^{0,2}$ are evaluated. For each rational model $S^{k,l}$, a corresponding fitness value $\delta_{k,l}$ is calculated in two steps. First, the distance of $S^{k,l}$ from all other current

interpolants is calculated at all $f \in \Gamma$ as

$$\Lambda_{k,l} = \sum_{\forall (m,n) \neq (k,l)} \left| S^{m,n}(f) - S^{k,l}(f) \right| \quad \forall\, (k,l). \tag{2.17}$$

Second, $\delta_{k,l}$ is calculated using

$$\delta_{k,l} = \frac{1}{M-1} \max_{f \in \Gamma} \Lambda_{k,l}(f) \quad \forall\, (k,l), \tag{2.18}$$

where M represents the total number of possible pole-zero arrangements for the rational interpolant.

From a geometrical perspective, $\delta_{k,l}$ represents the maximum average distance of $S^{k,l}$ *w.r.t.* all other interpolants $(m,n) \neq (k,l)$. According to the earlier sub-section, rational interpolants that better approximate $\boldsymbol{g}_{EM}$ should lie relatively close to one another. In other words, their fitness $\delta_{k,l}$ must be numerically smaller as compared to the interpolants that are far from the given EM relationship $\boldsymbol{g}_{EM}$. In the subsequent stage, the algorithm sorts the interpolants in ascending order of their fitness and picks the first N interpolants.

An error criterion, which can be used to guide the algorithm, is then calculated using

$$\phi_{k_i,l_i} = \frac{1}{N-1} \max_{f \in \Gamma} \sum_{j \neq i} \left| S^{k_j,l_j}(f) - S^{k_i,l_i}(f) \right|, \quad \forall\, i,j = 0,\ldots,N-1. \tag{2.19}$$

Let ζ represent a user-specified model accuracy, which can help to formulate the termination condition for the algorithm B. The algorithm terminates when

$$\phi_{k_i,l_i} \leq \zeta, \quad \forall\ i = 0,\ldots,N-1. \tag{2.20}$$

The understanding here is that if all the short-listed N interpolants lie satisfactorily close to one another, then all of them can be expected to accurately model the EM

response $S(f)$. In practice, the algorithm picks the rational interpolant with the least ϕ_{k_i,l_i}. If the condition in (2.20) fails, the algorithm proceeds to the next stage, wherein an additional EM data is acquired/simulated and all the above steps are repeated. The process of selecting the next EM sample is described in the following sub-section.

2.7.4 Adaptive Sampling

As mentioned earlier, if the user-specified model accuracy is not achieved, the algorithm proceeds to the next stage. Before proceeding to the next stage, a new EM sampling frequency needs to be identified. Ideally, the new EM data (f_k, y_k) should potentially lead to a relatively accurate rational model in the next stage. A close inspection of (2.19) indicates that for each of the N best interpolants, the error criterion ϕ_{k_i,l_i} is associated with a specific frequency $f \in \Gamma$. In other words, corresponds to a frequency at which $S^{k,l}$ differs the most from $N-1$ other short-listed interpolants. Based on the minimax concept, frequency f^* is identified as

$$f^* = \arg \max_{\substack{k_i,l_i \\ f \in \Gamma}} \phi_{k_i,l_i}, \quad \forall\, i = 0, \ldots, N-1. \tag{2.21}$$

The new EM data point is then generated not necessarily at f^* but at some f_g, where f_g is an allowed grid point in the neighborhood of f^* (in a manner very much similar to the algorithm A). Further, the set of current EM sampling grids is updated as

$$\Sigma = \Sigma \cup \{f_g\}. \tag{2.22}$$

If all allowed grid points in the neighborhood of f^* have already been used up, then the allowed sampling grid in that neighborhood is halved. The data set Ω is updated as

$$\Omega = \Omega \cup \Psi, \tag{2.23}$$

where Ψ represents the newly added grids.

2.8 Proposed Multidimensional Adaptive Sampling Algorithm A

In the case of multidimensional modeling, the model responses (*e.g.* S-parameters) are functions of geometrical or physical parameters $\boldsymbol{x}$ in addition to frequency f. For ease of notation, a new vector $\boldsymbol{p} = [\boldsymbol{x}\ f]^T$ is introduced, where $\boldsymbol{p}$ represents the multidimensional design parameter space. While p_k represents the k^{th} model input (or k^{th} design parameter), $\boldsymbol{p}_k$ represents the input vector corresponding to k^{th} EM sample. Let $\boldsymbol{g}_{EM}(\boldsymbol{p})$ represent a generalized RF/microwave response to be modeled and $S^{u,v}(\boldsymbol{p})$ represent the corresponding rational approximation. A set of $u+v+1$ EM data with inputs $\{\boldsymbol{p}_k \mid 1 < k < u+v+1\}$ is needed to develop such an approximation. Assuming the data is available, the objective of multi-variable rational interpolation is to find polynomials $H_i(\boldsymbol{p})$ and $V_j(\boldsymbol{p})$ and corresponding coefficients a_i and b_j such that

$$S^{u,v}(\boldsymbol{p}_k) = \frac{a_0 + \sum_{i=1}^{u} a_i H_i(\boldsymbol{p}_k)}{1 + \sum_{j=1}^{v} b_j V_j(\boldsymbol{p}_k)}, \tag{2.24}$$

for all k, $k = 1, 2, ..., u+v+1$.

As can be seen in (2.24), the numerator and the denomiator of the rational functions contain u and v number of polynomial terms respectively. The polynomial terms H_i and V_j are mixed-terms of the input/design parameters. For example, the i_{th} polynomial term in the numerator H_i could be one of $p_1, p_2, p_1^2, p_1 p_2$ and so forth. Typically, the choice of the polynomial terms could depend on the modeling problem or on the implementation scheme, or on both. Based on the work of [19], the proposed multidimensional algorithm A first generates all possible mixed-terms of the design

parameters $p_1, p_2, ..., p_n$ and sorts the terms in an ascending order of their degree. In a given stage, where rational approximation $S^{u,v}$ is being developed, the proposed algorithm selects the first u and the first v number of mixed-terms for the numerator and the denominator respectively. It is to be noted that the afore-mentioned sorting could be performed in several ways leading to multiple $S^{u,v}$ for a given u and v. This observation is exploited to indirectly contribute to the convergence of the proposed algorithm. In other words, when a particular sorting strategy fails to result in a user-specified model accuracy, other sorting schemes can be tried before exiting the algorithm.

As mentioned in Section 2.6, incorporation of the dynamic grid concept potentially avoids over-sampling in certain design sub-spaces. As such, adaptive sampling based on the new dynamic grid is integrated with standard multidimensional modeling technique [19] resulting in the proposed algorithm A. In each stage of the proposed algorithm A, two of the several possible rational functions, $S_m(\boldsymbol{p})$ and $S_{m-1}(\boldsymbol{p})$ of orders m and $m-1$ respectively, are selected and their coefficients are determined. The point $\boldsymbol{p}$, which happens to be the point of biggest mismatch between $S_m(\boldsymbol{p})$ and $S_{m-1}(\boldsymbol{p})$ is identified. The new EM data/sample is generated at a corresponding grid location $\boldsymbol{p}_g$, which lies on the dynamic grid. A systematic framework of the proposed multidimensional sampling algorithm A is shown in Fig. 2.4. The pseudocode of the proposed algorithm is presented below.

Let user-input $\boldsymbol{p} \subset \Re^d$ represent the design subspace where d denotes the dimension of design parameters including frequency. User input also includes desired model accuracy E_d and number of maximum allowed iterations k_d.

Initialization: Set $k = 1$. Initial grid-size is calculated as

$$\Delta_k^i = \frac{\max\{p_i\} - \min\{p_i\}}{2^{m_i}} \qquad i = 1, 2, ..., d. \tag{2.25}$$

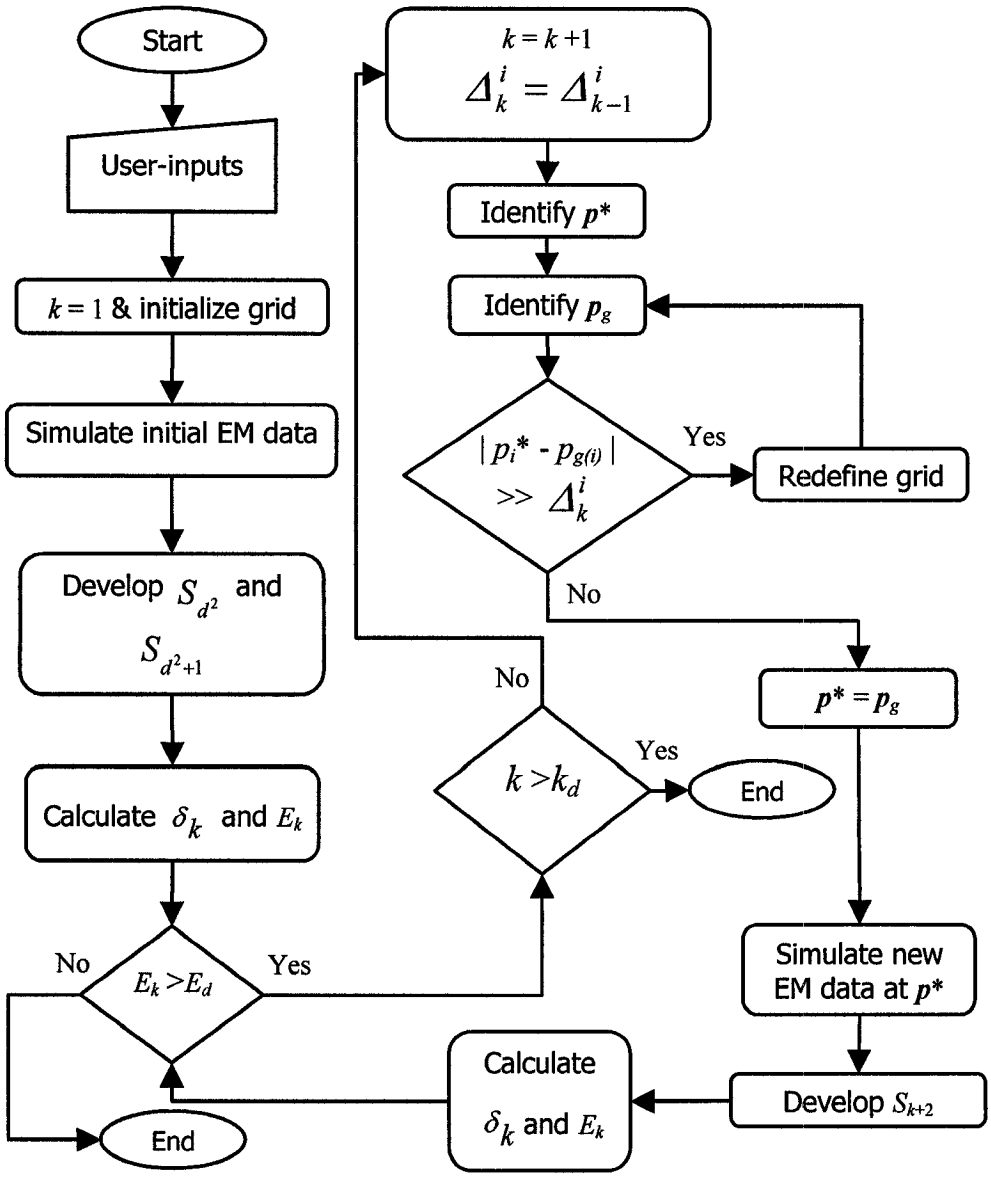

Figure 2.4: Systematic framework of the proposed multidimensional sampling algorithm A.

Using the above grid definition, the algorithm creates $2^{m_i}+1$ subinterval along each design parameter where m_i represents the number of intervals along the i^{th} dimension.

Stage 1: d^2 numbers of EM data are simulated in a star distribution within the $\boldsymbol{p}$ subspace without the centre point. A rational function of order S_{d^2} is developed based on current available samples. Then the centre point is simulated and the corresponding rational function of order S_{d^2+1} is developed. Residual function $\delta_{k=1}(\boldsymbol{p})$ at the end of the first stage is computed using a fine-grid and (2.26). Error E_1 is calculated using $\delta_{k=1}(\boldsymbol{p})$ and (2.27). If $E_1 > E_d$, then set $k = k+1$, otherwise STOP.

$$\delta_k(\boldsymbol{p}) = \frac{|S_{k+2}(\boldsymbol{p}) - S_{k+1}(\boldsymbol{p})|}{\max S_{k+2}(\boldsymbol{p}) - \min S_{k+2}(\boldsymbol{p})}. \tag{2.26}$$

$$E_k = \frac{1}{L}\left(\sum_{i=1}^{L} |\delta_k(\boldsymbol{p}_i)|\right). \tag{2.27}$$

Stage k: Set $\Delta_k^i = \Delta_{k-1}^i$. The new point around which $\boldsymbol{p}^*$ new EM data point need to be simulated is identified using (2.28). In the array of possible sample locations, unused design parameter grid $\boldsymbol{p}_g$ closest to $\boldsymbol{p}^*$ is located. If there exist a dimension (i) where $|p_i^* - p_{g_i}| >> \Delta_k^i$, then GO TO *RedefineGrid*, otherwise set $\boldsymbol{p}^* = \boldsymbol{p}_g$. Simulate EM data at $\boldsymbol{p}^*$. Set $k = k+1$. GO TO *ConvergenceCondition*.

$$\boldsymbol{p}^* = \arg\max_{\boldsymbol{p}} \{\delta_k(\boldsymbol{p})\}. \tag{2.28}$$

RedefineGrid: Set $m_i = m_i+1$ for dimensions where $|p_i^* - p_{g_i}| >> \Delta_k^i$, re-evaluate and update the array of possible sample locations. Unused grid frequency $\boldsymbol{p}_g$ closest to $\boldsymbol{p}^*$ is located. If $|p_i^* - p_{g_i}| >> \Delta_k^i$, then GO TO *RedefineGrid*, otherwise set $\boldsymbol{p}^* = \boldsymbol{p}_g$. RETURN Δ_k^i and $\boldsymbol{p}^*$.

ConvergenceCondition: If $k > k_d$ and all the different sortings have not been used up, then change the sorting of mixed-terms polynomials and GO TO stage 1. If $k > k_d$ and all the different sortings have been used up GO TO STOP. If $k < k_d$ then

GO TO *CheckTerminationCondition.*

CheckTerminationCondition: Residual function $\delta_k(\boldsymbol{p})$ at the end of the k^{th} stage is computed using a fine-grid, based on which E_k is calculated. If $E_k > E_d$, then set $k = k + 1$ and GO TO stage k, otherwise STOP.

The proposed multidimensional modeling algorithm A is purely based on rational functions. One of the key steps in the algorithm involves substituting the EM data into equations of the form (2.24) leading to a system of linear equations and solving for the coefficients. It is to be noted that the matrix of linear equations is relatively larger than the 1D modeling case, and is relatively more likely to be ill-conditioned [34]. Although in the proposed multidimensional algorithm A, the matrix conditioning is expected to be improved through the use of dynamic grid, the proposed algorithm A is less likely to be able to model cases where the model-resposne is highly non-linear along certain axis [19]. One way to address this difficulty is to resolve the system of equations into several sub-systems of lower-order [37]. Motivated by this challenge, multidimensional modeling algorithm B is proposed. In contrast to multidimensional algorithm A which solely uses rational functions, in proposed multidimensional algorithm B rational functions are utilized together with a hybrid mapping.

2.9 Proposed Multidimensional Adaptive Sampling Algorithm B

The multidimensional modeling problems can be divided into two categories. In the first category, there is no distinguishable highly non-linear design parameter. Such problems are already addressed in the proposed multidimensional algorithm A. In the second category, the model-input can be divided into two sub-spaces namely highly non-linear and less non-linear. Proposed multidimensional algorithm B is applied

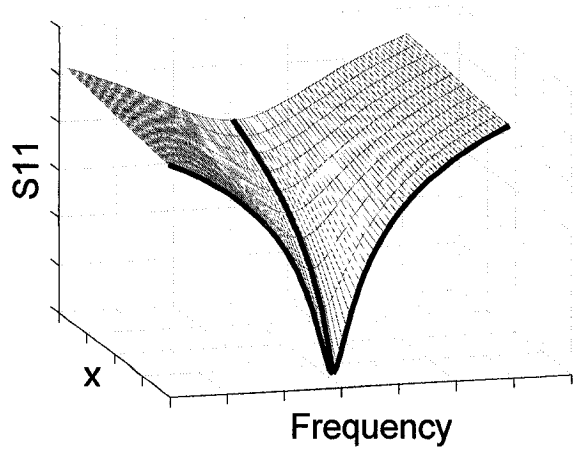

Figure 2.5: A typical multi-dimensional RF/microwave behavior.

to the second category of modeling problems. The division of model-input into two sub-spaces enables the proposed algorithms B to further reduce the number training EM samples in comparison to proposed algorithm A.

2.9.1 Motivation

Consider the 3D graph of Fig. 2.5 that represents a typical multidimensional S-parameter response of a high-frequency component. Two of the three dimensions represent the input parameters (x, f) and the third dimension represents the output (y). From the highlighted curves, it can be observed that $y = S_{11}$ is relatively more non-linear along one of the inputs f. Motivated by this typical RF/microwave tendency, a decomposition approach is employed, in which, a multidimensional input-space is divided into highly non-linear and less non-linear sub-spaces. The two sub-spaces can be addressed separately in two different phases of the proposed algorithm B.

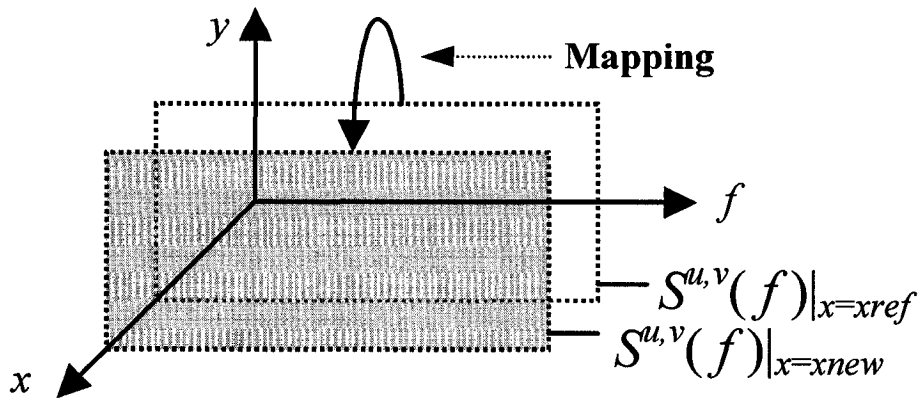

Figure 2.6: Conceptual representation of a general mapping problem.

2.9.2 Phase 1: Development of a Rational Sub-Model

The objective of Phase 1 is to develop a rational sub-model representing the RF/microwave behavior along the highly non-linear input (say f). This model will be developed for a fixed value of other inputs $\boldsymbol{x} = \boldsymbol{x}_{ref}$. By doing so, the multidimensional problem is simplified to the form of a single dimension problem. Using proposed algorithm B in section 2.7, $S^{u,v}(f)|_{x=x_{ref}}$ represent a rational sub-model approximating the S-parameter of interest in the reference plane *i.e.* $\boldsymbol{x} = \boldsymbol{x}_{ref}$.

2.9.3 Phase 2: Development of a Hybrid Mapping

This phase is motivated by the space-mapping concept [35] and the work of [16]. The objective of Phase 2 is to develop a set of rational sub-model which satisfactorily represent the given RF/microwave behavior at any new $\boldsymbol{x} = \boldsymbol{x}_{new}$ *i.e.* $S^{u,v}(f)|_{x=x_{new}}$ As such, Phase 2 is a sub-routine, which will repeat until a minimal set of rational sub-models that accurately emulate $\boldsymbol{g}_{EM}$ in the entire $(\boldsymbol{x}, f)$ space of interest. More specifically, in each repetition of Phase 2, a set of EM data at $\boldsymbol{x}_{new}$ is used to map $S^{u,v}(f)|_{x=x_{ref}}$ (of Phase 1) to $S^{u,v}(f)|_{x=x_{new}}$. Fig. 2.6 and Fig. 2.7 together illustrate the proposed hybrid concept, which maps a highly non-linear sub-model along a

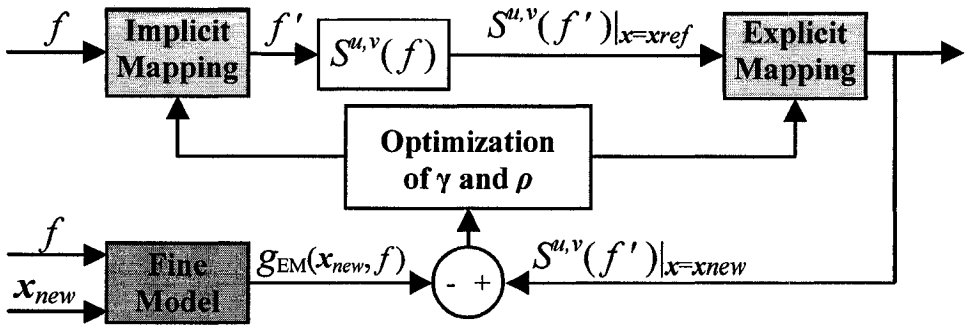

Figure 2.7: A block diagram showing Phase 2 of the proposed algorithm.

relatively less non-linear input dimension.

An inspection of the EM models at $\boldsymbol{x}_{ref}$ and $\boldsymbol{x}_{new}$ indicates that they are not only "shifted" but also "scaled" *w.r.t.* one another. This aspect must be considered while developing $S^{u,v}(f)|_{x=x_{new}}$ from $S^{u,v}(f)|_{x=x_{ref}}$. A hybrid mapping is proposed that unifies implicit and explicit mappings P and Q such that

$$f' = P(f) \tag{2.29}$$

and

$$S^{u,v}(f)|_{x=x_{new}} = Qo((S^{u,v}(f'))|_{x=x_{ref}}. \tag{2.30}$$

Considering that Phase 2 focuses on mappings along the less non-linear input axes, both P and Q can be defined as Taylor series expansions of orders ξ and η respectively *i.e.*

$$f' = P(f) = \gamma_0 + \gamma_1 f + \cdots + \gamma_{\xi-1} f^{\xi} \tag{2.31}$$

and

$$\begin{aligned} S^{u,v}(f)|_{x=x_{new}} &= Qo((S^{u,v}(f'))|_{x=x_{ref}}) \\ &= \rho_0 + \rho_1 (S^{u,v}(f)|_{x=x_{ref}}) + \cdots + \rho_{\eta-1} (S^{u,v}(f')|_{x=x_{ref}})^{\eta} \end{aligned} \tag{2.32}$$

Here, γ_i's and ρ_i's are unknowns. The initial mappings are set to be $\gamma_1 = 1$, $\rho_1 = 1$ while all other unknowns are zero. Consider

$$(\boldsymbol{\gamma}^*, \boldsymbol{\rho}^*) = \arg\min_{(\boldsymbol{\gamma},\boldsymbol{\rho})} \sum_{k=1}^{q} \| \boldsymbol{g}_{EM}(\boldsymbol{x}_{new}, f_k) - S^{u,v}(f)|_{\boldsymbol{x}=\boldsymbol{x}_{new}} \| \tag{2.33}$$

where q is the number of uniformly spaced frequency samples at $\boldsymbol{x} = \boldsymbol{x}_{new}$ and f_k is the k^{th} sampling location. Based on (2.33), the coefficients are optimized such that $S^{u,v}(f)|_{\boldsymbol{x}=\boldsymbol{x}_{new}}$ accurately represents $\boldsymbol{g}_{EM}(x_{new}, f)$. Finally, phase 2 is repeated for every optimization iteration to further minimize the required number of EM samples. In few cases where the algorithm in phase 2 does not converge for $\boldsymbol{x} = \boldsymbol{x}_{new}$, phase 1 is applied to $\boldsymbol{x} = \boldsymbol{x}_{new}$ and then $\boldsymbol{x} = \boldsymbol{x}_{new}$ is replaced with $\boldsymbol{x} = \boldsymbol{x}_{ref}$.

2.10 Numerical Results

In a typical RF and microwave component response, S_{11} which represents matching, often shows a relatively highly non-linear *w.r.t.* frequency. Hence, in all the following examples in this chapter, S_{11} is considered as model response.

2.10.1 Band-Pass Filter

In this example the performance of the 1D standard algorithm is compared with the proposed 1D algorithms A and B. Left-handed microwave structures are gaining attention, and accurate EM based modeling of such structures is important. In this example, a band-pass filter consisting of a left-handed microstrip transmission line offering the benefits of compact-size and low-loss is modeled. The geometry of the band-pass filter is shown in Fig. 2.8. Data required for modeling the filter is obtained from an EM simulator, namely Zeland's *IE3D*.

The frequency response of the filter is highly nonlinear in the [3, 13]GHz range. Conventional modeling based on non-adaptive uniform-grid is expensive, and the stan-

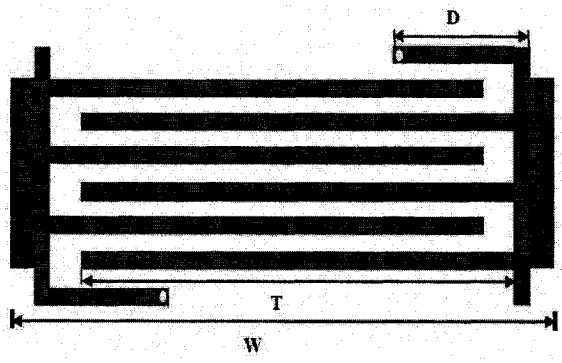

Figure 2.8: Geometry of the left-handed transmission line band-pass filter with $D = 0.8mm, T = 3.925mm$ and $W = 4.425mm$ from [16].

dard algorithm gets trapped in the vicinity of $f = 9.15$GHz as seen in Fig. 2.9(a). At the end of the 22^{nd} stage, it is observed that the standard model completely misses the resonant frequency $f = 7.14$GHz. At this stage, the average error between the best and the second best models is 8%. The best model is compared with EM data, and the average error is found to be $14.67\% > E_d = 10\%$. Continuing further with 14 additional stages (using 14 extra EM data) leads to an improvement in the above errors to 4.8% and 12.46% respectively, which is not considerable.

Alternatively, the proposed algorithm A is applied. After 22 stages, the algorithm results in a model with $E_{22} = 3.55\%$. The model is compared with the EM data, and the average error calculated by (2.12) is observed to be an acceptable 5%. The response of the proposed model versus EM data is shown in Fig. 2.9(b). Finally, the proposed algorithm B is applied. After using 20 EM data, the algorithm results in a rational model $S^{8,11}$ with error criterion $\phi_{8,11} = 5.27\%$. This model is compared with EM data (Fig. 2.9(c)) and the average error in this case is observed to be an acceptable 8.34%. For this example alone, algorithm A resulted in a relatively better model than algorithm B.

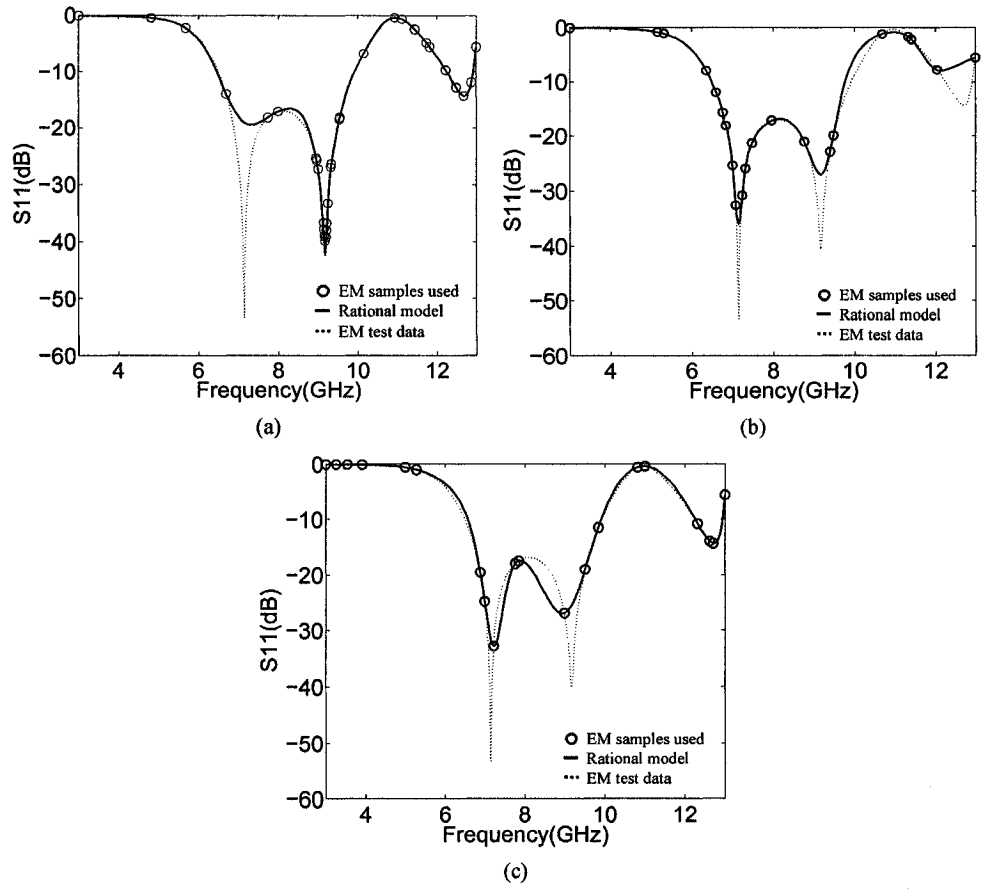

Figure 2.9: Frequency response of the filter's rational model developed using (a) standard algorithm after 36 stages, (b) proposed algorithm A after 22 stages, (c) proposed algorithm B after 20 stages (all represented by solid lines), and the EM test data used for model validation (dotted lines). Circular dots represent the distribution of the frequency samples used by the respective algorithms.

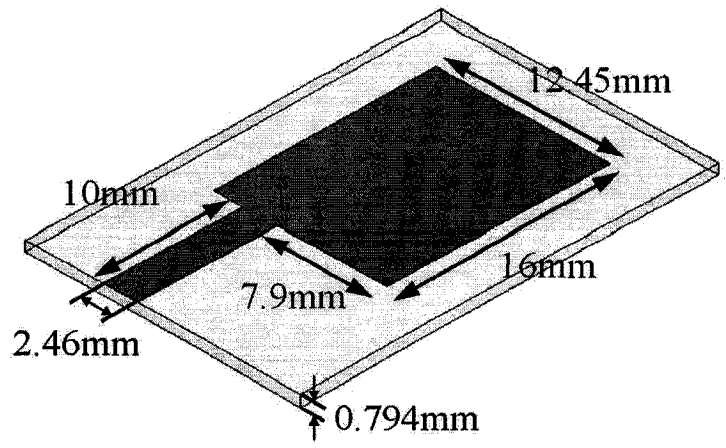

Figure 2.10: Geometry of the microstrip patch antenna from [16].

2.10.2 Patch Antenna

In this example the performance of the 1D standard algorithm is compared with the proposed 1D algorithms A and B. In high-performance aircraft and missile applications, where size and weight are critical, microstrip patch antennas are preferred. In this example, rational function models of a patch antenna are developed. The geometry of the antenna is shown in Fig. 2.10. EM data required for modeling are obtained from Ansoft's *HFSS*. User-specifications are $f_{min} = 5\text{GHz}$, $f_{max} = 20\text{GHz}$, and $E_d = 5\%$. The presence of several resonant frequencies in this frequency range leads to interesting results.

Conventional modeling based on non-adaptive uniform-grid distribution requires a large number of EM data points and is hence computationally expensive. The standard algorithm is observed to get trapped in the proximity of $f = 7.52\text{GHz}$. At the end of the 40^{th} stage, it is observed that the standard model completely misses the resonant frequency $f = 18.17\text{GHz}$. At this stage, the average error between the best and the second best models is 7.8%. The best model is compared with the EM data, and the average error is observed to be 12.5%. Continuing further with 20 additional

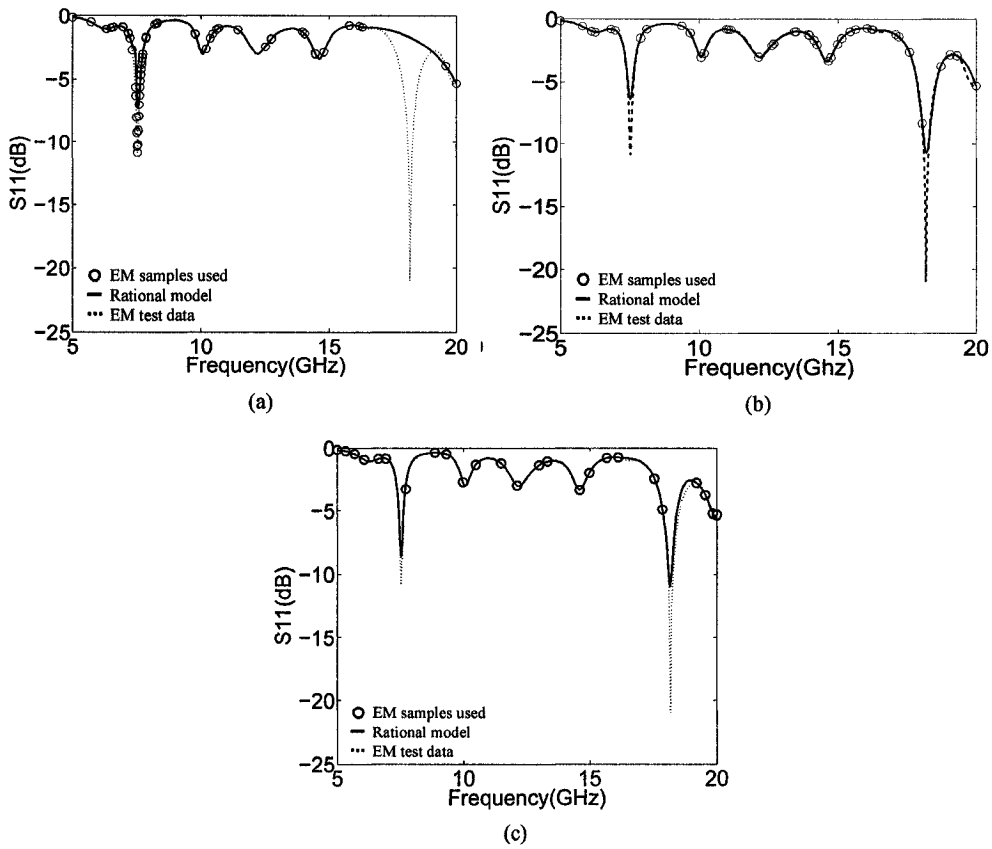

Figure 2.11: Frequency response of the antenna's rational model developed using (a) standard algorithm after 60 stages, (b) proposed algorithm A after 41 stages, (c) proposed algorithm B after 25 stages (all represented by solid lines), and the EM test data used for model validation (dotted lines). Circular dots represent the distribution of the frequency samples used by the respective algorithms.

Table 2.2: Comparison of the model accuracies for the patch antenna

No. of EM Data	Error Between the Best and the Second Best Rational Approximations		Error Between the Best Rational Approximation and the EM Data		
	Standard Algorithm	Proposed Algorithm A	Standard Algorithm	Proposed Algorithm A	Proposed Algorithm B
24	9.9%	24.5%	17.5%	26.4%	5.1%
30	8.2%	9.7%	16.2%	10.5%	4.8%
36	7.8%	6.0%	14.8%	8.6%	4.8%
38	7.8%	4.8%	12.9%	4.9%	4.0%
42	7.8%	4.0%	12.5%	4.5%	3.8%

stages still fails to help detection of the missed resonant frequency (See Fig. 2.11(a)).

Alternatively, the proposed algorithm A is applied. After 40 stages, the algorithm results in a model with $E_{40} = 4\%$. The model is compared with the EM data, and the average error is observed to be an acceptable 4.5%. The frequency response of the proposed model versus EM data is shown in Fig. 2.11(b). Finally, the proposed algorithm B is applied. After using 25 EM data, the algorithm results in a rational model $S^{9,15}$ with error criterion $\phi_{9,15} = 5.37\%$. For the purpose of validation, this model is compared with the EM data (Fig. 2.11(c)), and the average error is observed to be $4.9\% < E_d = 5\%$. The proposed algorithm B uses 15 fewer EM data than the algorithm A and achieves almost equal model accuracy. The stage-wise model errors presented in Table 2.2 demonstrate the effectiveness of the proposed algorithms *w.r.t.* the standard algorithm.

2.10.3 Waveguide Filter (One-Dimension)

In this example the performance of the 1D standard algorithm is compared with the proposed 1D algorithms A and B. A waveguide with a cross-section of 1.372" $\times$ 0.622"

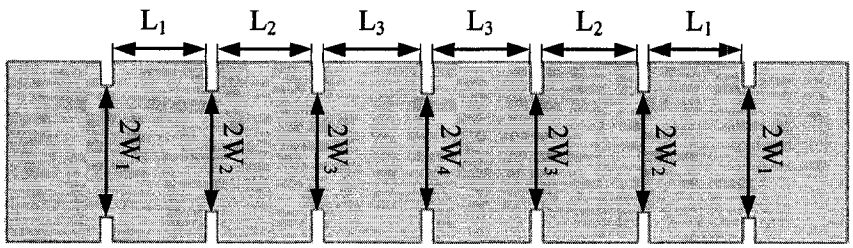

Figure 2.12: Geometry of the H-plane wave guide filter from [7].

Table 2.3: Geometry values of the H-plane wave guide filter from [7].

Parameters	Geometry(in inches)
W_1	0.499802
W_2	0.463828
W_3	0.44544
W_4	0.44168
L_1	0.630762
L_2	0.644953
L_3	0.665449

(or $3.485cm \times 1.58cm$) is used [7]. The six sections (See Fig. 2.12) are separated by seven-plane septa, which have a finite thickness of 0.02" (or $0.508mm$). The values corresponding to the geometry of the waveguide filter are shown in Table 2.3. EM data are obtained from Ansoft's *HFSS*. The frequency response of the filter is highly nonlinear in the [5.5GHz, 8.5GHz] GHz range.

Conventional modeling based on non-adaptive uniform-grid is expensive, and the standard algorithm gets trapped in the vicinity of $f = 8.5$GHz as seen in Fig. 2.13(a). At the end of the 60^{th} stage, it is observed that the standard model completely misses the resonant frequency at $f = 5.76$GHz. The average error between the best and the second best models is 8%. The best model is compared with EM data, and the average error is found to be an unacceptable $14.67\% > E_d = 10\%$.

Alternatively, the proposed algorithm A is applied. As it can be seen in Table 2.1, the condition numbers, using Chebyshev and Legendre, are highly improved in com-

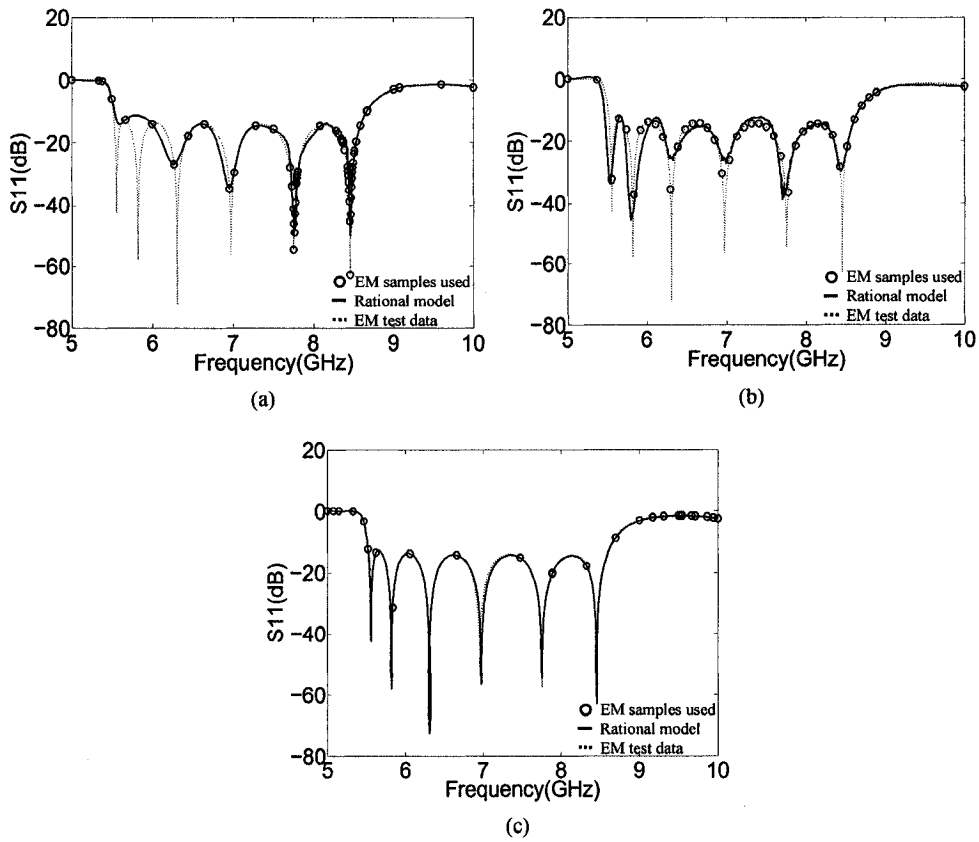

Figure 2.13: Frequency response of the waveguide's rational model developed using (a) standard algorithm after 60 stages, (b) proposed algorithm A after 40 stages, (c) proposed algorithm B after 25 stages (all represented by solid lines), and the EM test data used for model validation (dotted lines). Circular dots represent the distribution of the frequency samples used by the respective algorithms.

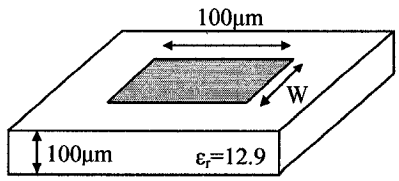

Figure 2.14: The Geometry of the open-stub microstrip.

pare to the ones with monomial bases. After 40 EM samples, the algorithm results in a model with $E_{38} = 3.55\%$. The model is compared with the EM data, and the average error, calculated by equation (2.12) is observed to be $9.78\% < E_d$. The response of the proposed model versus EM data is shown in Fig. 2.13(b). Finally, the proposed algorithm B is applied. After using 25 EM data, the algorithm results in model $S^{14,10}$ with $\phi_{14,10} = 4.67\%$. This model is compared with EM data (Fig. 2.13(c)), and the average error is observed to be 5.14%. In this example, algorithm B uses 15 fewer EM data than algorithm A, while achieving significantly improved model accuracy. Extra computation time used by the algorithm B for selecting "closely bounded rational models" can be neglected, since rational function evaluations are much simpler/faster than EM simulations.

2.10.4 Open-Stub Microstrip

This example compares the proposed multidimensional algorithm A with the standard multidimensional algorithm. An open-stub microstrip on a $100\mu m$ GaAs substrate with $\epsilon_r = 12.9$ is considered. The geometry of the open-stub is shown in Fig. 2.14. The model outputs are S-parameters. In this example itself, illustrative graph showing one of the outputs to be modeled *i.e.* $\mathrm{Re}[S_{11}]$ is shown in Fig. 2.15. Design parameters that are involved in the modeling are the width of the strip W and frequency f. The width of the strip and frequency intervals which the model is generated

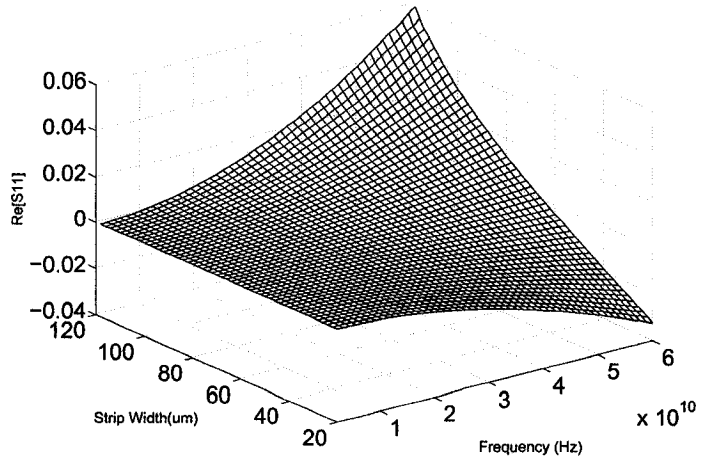

Figure 2.15: Real part of S_{11} for the open-stub microstrip.

upon are $[20\mu m, 118\mu m]$ and [2GHz, 60GHz] respectively. Model accuracy (E_d) and convergence criterion (k_d) are adjusted to 0.005% and 50 respectively. Data required for modeling the microstrip is obtained from a well known EM simulator, namely Agilent's *ADS*.

The standard multidimensional modeling algorithm is applied. In the first iteration, EM simulations are carried out for the star distribution of EM samples *i.e.* (2GHz, $68\mu m$), (30.41GHz, $118\mu m$), (60GHz, $68\mu m$) and (30.41GHz, $20\mu m$). These initial samples result in a rational function of order 4 (S_4). In the next step, the simulation for the centre point *i.e.* (30.41GHz, $68\mu m$) is executed and the second rational function of order 5 (S_5) is generated. The next sample is precisely selected at the location of biggest mismatch between two previously generated rational models *i.e.* S_4 and S_5. Proceeding further with 20 samples, the algorithm reaches the average accuracy of -72dB ($E_{16} = 0.0002\%$). The error between the fine EM data and rational model after 20 samples is shown throughout the design space in Fig. 2.16(a). EM sample distribution shows regions that samples are unnecessarily selected in the vicinity of each other (see Fig. 2.16(b)).

Alternatively, the proposed multidimensional algorithm A is applied. The number

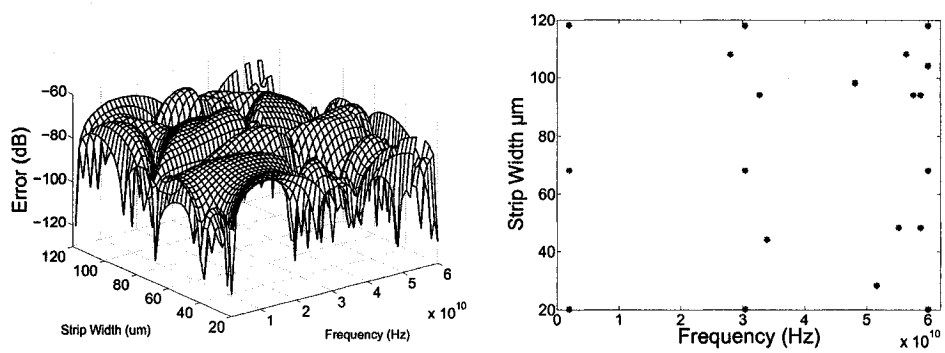

(a) (b)

Figure 2.16: (a) Error between fine data and approximated model generated by standard multi dimensional algorithm (b) EM sample distribution for Standard algorithm.

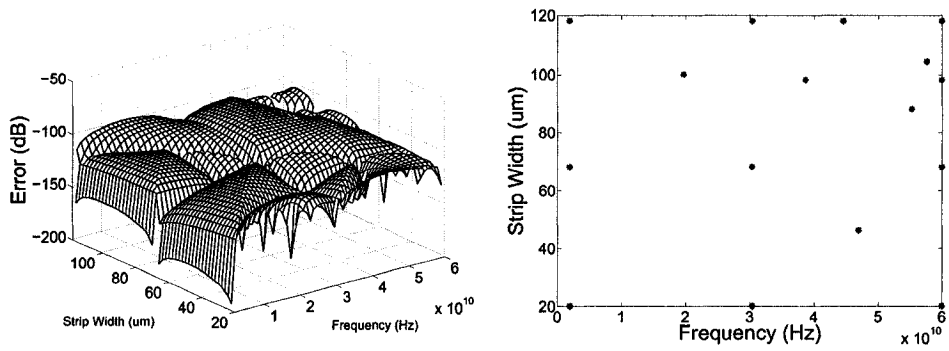

(a) (b)

Figure 2.17: (a) Error between fine data and approximated model generated by proposed multi dimensional algorithm A (b) EM sample distribution for proposed algorithm A.

of modeling parameters (d) is set to 2 corresponding to model parameters *i.e.* W and f. The initial number of grid intervals along frequency and strip width are set to $m_1 = 8$ and $m_2 = 4$ respectively. Starting with the star distribution of EM samples and generating the initial S_4 and S_5 rational models, new data point $\boldsymbol{p}^*$ at which a new data needs to be simulated is identified. New samples are selected at $\boldsymbol{p}_g$ on dynamic grid which is not necessary the same point of biggest mismatch. Proceeding further with 16 samples the average accuracy of -104dB ($E_{12} = 6.3 \times 10^{-6}\%$) is achieved. The error between the fine EM data and the rational model is shown throughout the design space in Fig. 2.17(a). EM sample distribution for the proposed multidimensional algorithm A shows no over-sampling at any unnecessary region (See Fig. 2.17(b)). It is observed that in the light of dynamic grid, the number of samples is reduced by 4 and yet the average model accuracy is improved by 32dB. This aspect is important in the case of recursive optimization algorithms for high performance component design.

2.10.5 Waveguide Filter (Multidimensional Algorithm A)

A waveguide filter of Fig. 2.12 is modeled using the proposed multidimensional algorithm A. The model-output is the amplitude of S_{11} which is relatively more non-linear in comparison to other scatering parameters. The model response using a fine EM simulation is shown in Fig. 2.18. The number of model-inputs is two including W_1 and f and their corresponding intervals of interest are $W_1 \in$ [0.38inch,0.48inch] and $f \in$ [5GHz,10GHz]. Model accuracy (E_d) and convergence criterion (k_d) are set to be 0.005% and 50 respectively. Data required for modeling the waveguide filter is obtained from a well known EM simulator, namely Ansoft's *HFSS*. The proposed multidimensional modeling algorithm A is applied. After 87 stages, the algorithm results in model S_{89} with $E_{87} = 0.004\%$. The model is compared with the EM data and the average error is observed to be an acceptable 0.0048%. The model errors in Table 2.4 clearly demonstrate the advantage of the proposed multidimensional algorithm A

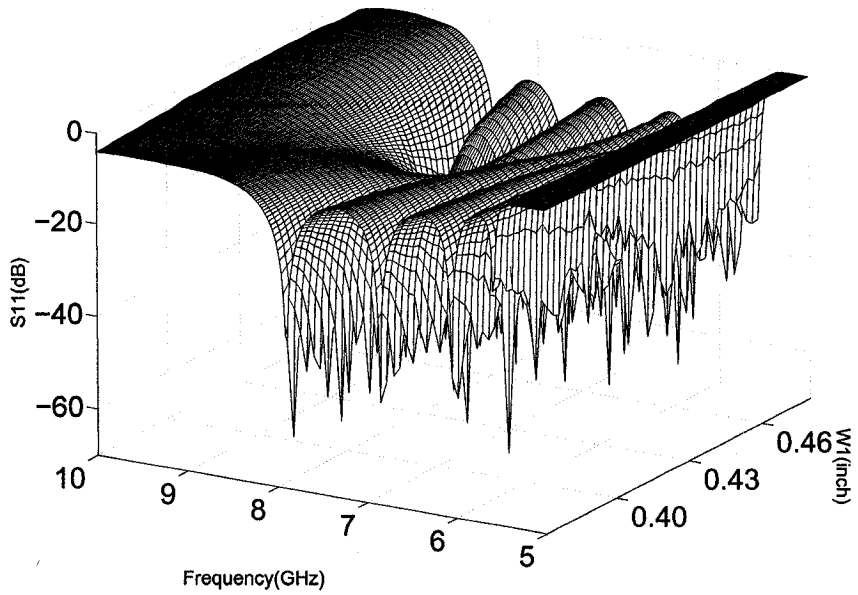

Figure 2.18: Model response of the waveguide filter using a fine EM simulation.

in comparison to the standard algorithm.

2.10.6 Waveguide Filter (Multidimensional Algorithm B)

In this section, a [5, 10] GHz waveguide filter of Fig. 2.12 is modeled using the proposed multidimensional algorithm B. The number of model inputs is 8 including 7 geometrical parameters of Table 2.5 and frequency. Table 2.5 presents the input regions over which the developed model is to be validated. It may be noted that these regions are bounded by the extremities of at least 2 of the 7 parameters. Hence, of the entire input space of interest, the RF/microwave behaviors in these regions are difficult to model. Simulations of Ansoft's *HFSS* are used as fine data.

In Phase 1, a rational sub-model is to be generated at $\boldsymbol{x}_{ref}$ (of Table 2.5) from an initial analytical design [7]. User-defined parameters $M = 4$ and $\zeta = 0.5dB$. After 25 iterations of Phase 1, *i.e.* $N = 25$, the termination condition in (2.20) is met. Evolution of $S^{u,v}(f)|_{\boldsymbol{x}=\boldsymbol{x}_{ref}}$ with increasing N is shown in Fig. 2.19. In Phase

Table 2.4: Comparison of the model accuracies for the waveguide filter.

Sample No.	Error Between the Best and the Second Best Rational Approximations		Error Between the Best Rational Approximation and the EM Data	
	Standard Algorithm	Proposed Algorithm A	Standard Algorithm	Proposed Algorithm A
59	0.1950%	0.1097%	0.5647%	0.1976%
69	0.1374%	0.0497%	0.3486%	0.0736%
79	0.0166%	0.0097%	0.3245%	0.0135%
89	0.0100%	0.004%	0.3142%	0.0048%

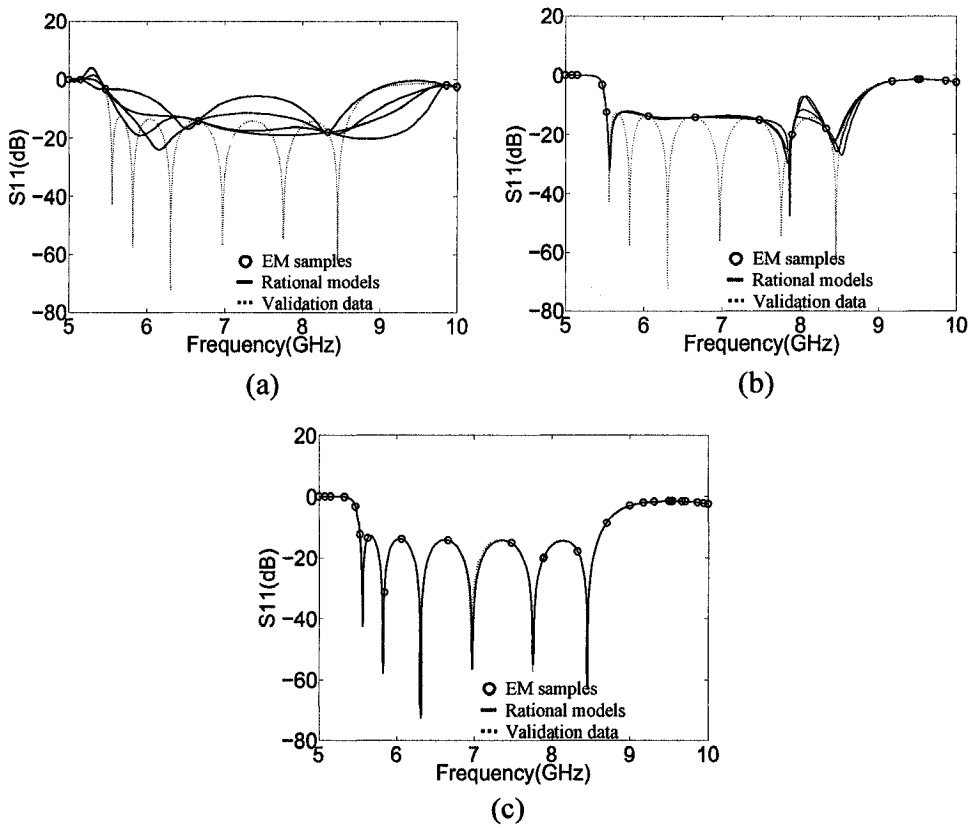

Figure 2.19: Evolution of the rational sub-model $S^{u,v}(f)|_{x=x_{ref}}$ as Phase 1 progresses through (a) 7, (b) 15 and (c) 25 iterations.

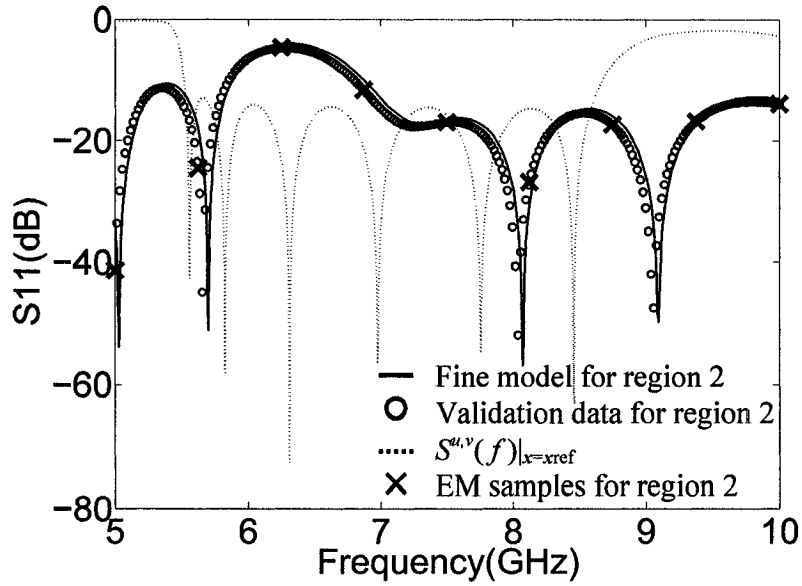

Figure 2.20: Sub-model for region 2 developed using Phases 1 and 2.

Table 2.5: Reference plane and validation regions

$\boldsymbol{x}$(inch)	$\boldsymbol{x}_{ref}$	Region 1	Region 2	Region 3
L_1	0.706	1.152	0.891	1.413
L_2	0.644	0.905	1.288	1.166
L_3	0.655	1.330	1.187	0.926
W_1	0.499	0.597	0.662	0.630
W_2	0.463	0.496	0.594	0.561
W_3	0.445	0.510	0.543	0.608
W_4	0.441	0.474	0.539	0.572

2, the order of the Taylor series' for both implicit and explicit mappings are set to $\xi = \eta = 3$. Reducing the number (q) of uniform frequency samples in the "$\boldsymbol{x} = \boldsymbol{x}_{new}$ plane" or "region 2" reduces the CPU-cost. Here, $q = 9$. Fig. 2.20 shows a result from Phase 2 corresponding to region 2. The hybrid mapping not only shifts and scales $S^{u,v}(f)|_{\boldsymbol{x}=\boldsymbol{x}_{ref}}$ but also detects/changes the number of resonant frequencies from 6 at $\boldsymbol{x}_{ref}$ to 4 at $\boldsymbol{x}_{new}$.

In the case where an advanced genetic concept based 1D rational modeling algorithm is used (see section 2.7), EM data in the order of N^8 will be required, since the 1D algorithm needs to repeat along all 8 input axes. The proposed multidimensional algorithm B, on the other hand, will require $N + q^8$ EM data. Since $q^8 << N^8$, the proposed algorithm B considerably reduces the number of EM data needed to develop a satisfactory model. Table 2.6 compares the proposed algorithm and the brute-force repetition of the 1D algorithm. The proposed multidimensional algorithm B uses 25 EM data to create the sub-model at $\boldsymbol{x} = \boldsymbol{x}_{ref}$ and 9 EM data to generate a sub-model for each additional validation region.

2.11 Summary

Enhanced frequency sampling algorithms for automatic development of EM-based RF/microwave rational interpolants have been proposed in both single and multidimensional problems. Starting with a minimal number of EM data and lowest-order rational functions, these algorithms iteratively build surrogate models, which satisfy user-specified model accuracies. The algorithms use relatively fewer samples than the standard algorithms to achieve similar model accuracies, and are hence cost-effective. Illustration examples show that in contrast to the standard algorithm, the proposed algorithms avoid over-sampling around critical regions and significantly reduce the number EM samples.

Table 2.6: Comparison between modeling algorithms

		Region 1		Region 2		Region 3	
		EM data used at $\boldsymbol{x} = \boldsymbol{x}_{new}$	Validation error	EM data used at $\boldsymbol{x} = \boldsymbol{x}_{new}$	Validation error	EM data used at $\boldsymbol{x} = \boldsymbol{x}_{new}$	Validation error
Proposed model	Max. Error	9	24.365 dB	9	27.232 dB	9	21.623 dB
	Mean Error		0.4196 dB		0.5870 dB		0.4132dB
Brute-force model	Max. Error	23	0.4055 dB	24	0.5067 dB	24	0.2954 dB
	Mean Error		0.4196 dB		0.5870 dB		0.2543 dB

Chapter 3

Space-Mapping-Based Temperature Modeling of Combline Resonators

3.1 Introduction

Frequency drift due to temperature changes is a key concern in RF/microwave filter performance. This aspect is particularly critical in the case of combline resonators (cylindrical cavities) used in a wide variety of RF/microwave systems. Several temperature compensation techniques exist. One such techniques involves the use of special materials with low thermal coefficients of expansion, *e.g.* invar. However, such materials could lead to other problems such as low thermal conductivity and high cost. It was also shown that for a combline resonator with given dimensions of housing and resonator rod, perfect temperature compensation can be achieved at two resonant frequencies through appropriate selection of materials for the housing and the rod [36]. Another recent temperature compensation method [37] advocated use of a shape memory alloy (SMA) actuator.

To be able to apply temperature compensation techniques such as the above to

RF/microwave filter design procedures, accurate and fast temperature drift models of combline resonators are essential. Simple relationships between the resonant frequency of a combline resonator and the temperature exist [37][38]. However, these empirical formulae are not accurate enough and fail to cover different rod structures *e.g.* those in Fig. 3.1. There is a demand for a reasonably accurate model, which takes into account all the geometrical aspects of a combline resonator.

A direct approach to address this problem is to use detailed theoretical models such as the full-wave EM solvers. In practice, full-wave EM simulations tend to be CPU-expensive and hence unsuitable for design/optimization tasks. This scenario motivates research on novel EM-based CAD models [39].

This chapter starts with literature review of available empirical formulae and numerical methods for temperature modeling of cavity resonators. Subsequently, a space-mapping-based CAD model which is fast and accurate is proposed. The robustness of the proposed model is illustrated through numerical examples.

3.2 Conventional Modeling

3.2.1 Empirical Model

In this section, an empirical model for the frequency drift of a combline resonator due to temperature is reviewed. In reality, it is the geometry of a cavity resonator that changes with temperature. As such, all the lengths such as cavity height and width change with respect to three factors: temperature drift, initial length and the thermal expansion coefficient of the material. In metals, which are allowed to expand freely, linear expansion can be assumed. It can be shown that the change in metal length ΔL is given by equation

$$\Delta L = \alpha L_i \Delta T, \tag{3.1}$$

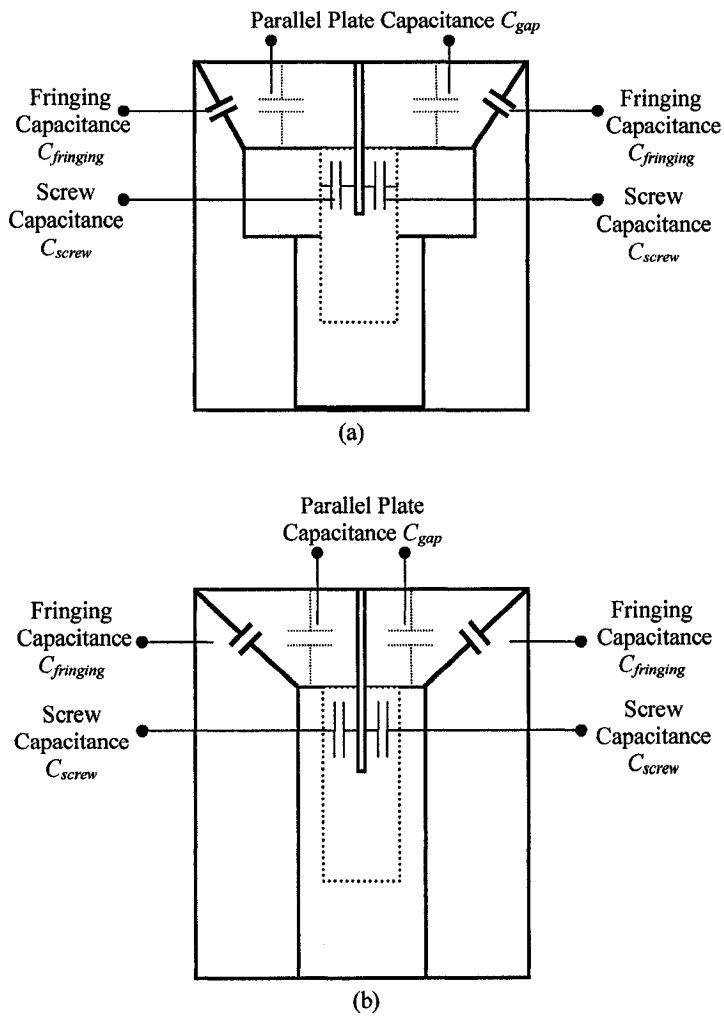

Figure 3.1: The gap capacitance C_{gap} and the equivalent screw capacitance C_{screw} are shown in (a) a Mushroom rod and (b) a straight rod resonator structure.

where α, ΔT and L_i are the thermal expansion coefficient (CTE), temperature change and the initial length respectively.

In some temperature compensation methods, designers try to achieve an effective CTE, which is not naturally available. In such cases, two pieces of metals are attached. Depending upon the length of each piece, the equivalent CTE for the combined part lies within the CTE's of the two attached metals. The equivalent CTE (ϑ) for such a part can be calculated as

$$\vartheta = \frac{a_1}{a_1 + b_1}\alpha + \frac{b_1}{a_1 + b_1}\beta, \tag{3.2}$$

where α and β are the CTEs for two metals and a_1 and b_1 are the initial lengths respectively.

According to [37], based on free expansion assumption, it can be easily shown that the resonant frequency of a conductor-loaded rectangular cavity following a ΔT temperature change can be calculated by

$$f(\Delta T) = \frac{c\sqrt{a_0^2(1+\alpha\Delta T)^2 + d_0(1+\alpha\Delta T)^2}}{1 + a_0 d_0(1+\alpha\Delta T)^2} \approx f_0 \frac{1}{1+\alpha\Delta T}, \tag{3.3}$$

where f_0 is the resonant frequency of the unperturbed resonator and a_0, b_0 and d_0 represent the length, width and height of the rectangular cavity resonator respectively ($b_0 < a_0 < d_0$). Although [37] claims that equation (3.3) achieves high accuracy for different structures, *i.e.* reentrant coaxial resonator, disk resonator and half cut resonator, it can be easily observed that (3.3) does not distinguish between a conducted-loaded cavity and a simple unperturbed rectangular waveguide cavity. Besides, EM simulations in [36] also shows that (3.3) is not valid for other structures and does not represent a reliable model for temperature behavior of combline resonators with different structures *e.g.* mushroom.

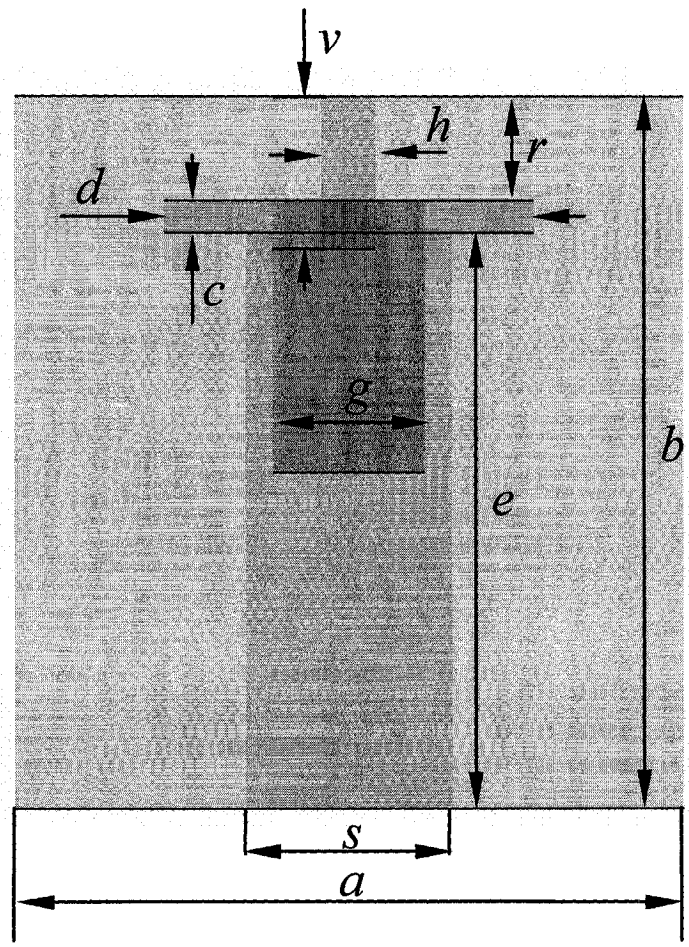

Figure 3.2: A mushroom rod cylindrical combline cavity shown with designable dimensions.

3.2.2 Circuit Model

In this section, a simple equivalent circuit for a combline resonator is reviewed. An idealized circuit model for a combline resonator is a coaxial transmission line, which is loaded by three types of capacitances namely parallel plate (gap) capacitance C_{gap} , screw capacitance C_{screw} and fringing capacitance $C_{fringing}$ [38] (See Fig. 3.1). Accordingly, the the quality of temperature modeling depends upon how accurately these three capacitances are calculated. Since these capacitances are in parallel, the total effective loaded capacitance can be calculated using

$$C_e = C_{gap} + C_{screw} + C_{fringing}. \tag{3.4}$$

Different empirical formulae have been presented to approximate all the components of loaded capacitance C_e. Martin [38] approximates the parallel plate capacitance C_{gap} by

$$C_{gap}(pF) = \frac{0.00885\pi d^2}{4r}, \tag{3.5}$$

where r and d are the gap and the diameter of mushroom rod both in mm (See Fig. 3.2).

Nicholson [40] presents a simple linear function using Whinnery *et al*'s data [41], for calculating fringing capacitance of a mushroom rod. This fringing capacitance can be approximated over a certain range as

$$C_{fringing}(pF) = 0.0275d \qquad where \qquad \frac{s}{a} < 0.5, \tag{3.6}$$

where d, s and a are the diameter of mushroom rod in mm, cavity diameter and rod diameter respectively as shown in Fig. 3.2.

Somlo [41] also presents a more accurate relationship for fringing capacitance ($C_{fringing}$) using Taylor series of degree two to fit the same set of data. The final

Taylor expression is given by

$$C_{fringing}(pF) = 0.0013a + 0.0164d + 0.0183\frac{d^2}{a}, \tag{3.7}$$

where a and d are the outer diameter and mushroom rod diameter in mm shown in Fig. 3.2. Equations (3.6) and (3.7) treat the resonator terminated in an open circuit without the assumption of an end wall. The equations are only valid for relatively large gaps (r) and if the gap is small, the effect of C_{gap} becomes more dominant and hence the effect of $C_{fringing}$ can be neglected.

The behavior of tuning screw capacitance is hard to be described mathematically. Depending on the position of the tuning screw which is not a known *a priori*, a combline resonator shows various temperature behaviors. Despite this difficulty, according to [38], reasonable accuracy can still be obtained by choosing one of two possibilities given below.

1. The screw diameter (h) is small relative to the outer diameter of the combline resonator (a). In this case, the effective height of the cavity can vary proportionally with the length of the screw. In other words, adjusting the depth of the tuning screw effectively changes the cavity height. This change in cavity height leads to change in the effective gap and consequently changes the effective gap capacitance.

2. The screw diameter is considerable in comparison with the outer diameter of resonator. In this case, in addition to a change in the effective height of cavity, the tuning screw results in a cylindrical capacitance (C_{screw}) with the outer walls of the combline resonator. This cylindrical capacitance can be calculated by

$$C_{screw} = \frac{2\pi\epsilon_0}{\ln(\frac{a}{h})}v, \tag{3.8}$$

where v, a and h are the screw penetration inside the cavity, cavity diameter

and screw diameter respectively (See Fig. 3.2).

After calculating the effective capacitance (C_e), employing the above formulae, the centre frequency can be determined using

$$f = \frac{1}{2\pi C_e Z_0 \tan\theta}, \tag{3.9}$$

where Z is the estimated characteristic impedance of the straight rod combline resonator, C_e is the total loading capacitance, θ is the electrical length of rod and f is the centre frequency of the resonator. In a combline resonator with a straight rod, Z_0 is given by

$$Z_0 = 60\ln(\frac{a}{s}), \tag{3.10}$$

where a and k are the cavity diameter and rod diameter respectively. Martin [38] modifies (3.10) and offers another formula for the characteristic impedance of a mushroom rod combline resonator *i.e.*

$$Z_0 = 60\ln(\frac{4a}{\pi s}), \tag{3.11}$$

Although this method is widely being used in industry for straight structures, it is not accurate enough for other structures such as mushroom.

3.3 Motivation for Space Mapping

Although empirical formulae are fast and easy to compute, they are not accurate for arbitrary rod structures such as mushroom. This imprecision is due to inaccurate estimation of loading capacitances and not taking into account the fringing effects [38]. Commercial EM solvers are alternatives to modeling the temperature behavior of combline resonators. Although full-wave methods can accurately determine the temperature behavior of combline resonators, they are slow and CPU-expensive. As

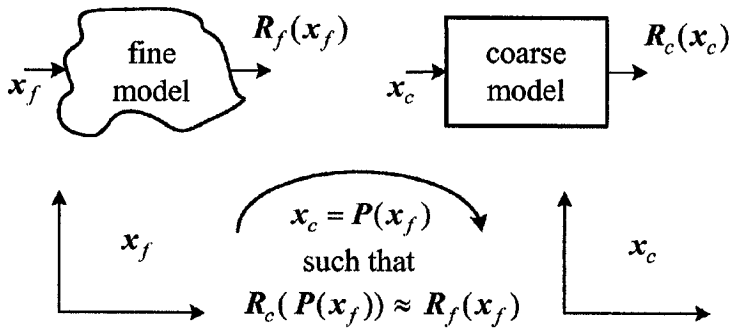

Figure 3.3: Overview of space mapping [42].

such they are not practical for design and optimization, which require repetitive simulations.

Space mapping [42] effectively connects the efficiency of empirical formulae (coarse models) to the accuracy of the EM simulators (fine models). Space mapping yields a surrogate model which is reasonably accurate and fast to evaluate. The generated model then can be exploited by design and optimization algorithms.

3.3.1 Review of Space Mapping

The fundamental concept of space mapping is to match the response of the coarse and fine models by establishing an input mapping as shown in Fig. 3.3 [42]. Once again, coarse model is typically a computationally fast circuit-based model which does not take into account detailed electromagnetic effects, whereas the fine model is a CPU-intensive full-wave EM simulation.

In Fig. 3.3, $\boldsymbol{x}_c \in X_c$ stands for coarse model parameters and $\boldsymbol{x}_f \in X_f$ stands for fine model design parameters. $X_c \subset \Re^{n\times 1}$ and $X_f \subset \Re^{n\times 1}$ are coarse model and fine model parameter spaces of n design parameters. The corresponding vectors of m responses (*e.g.*, $|S_{21}|$ at m different frequency points) for the coarse model and fine model are denoted as $R_c \subset \Re^{m\times 1}$ and $R_f \subset \Re^{m\times 1}$, respectively. The original design

problem can be formulated as

$$\boldsymbol{x}_f^* \equiv \arg\min_{\boldsymbol{x}_f} U(R_f(\boldsymbol{x}_f)), \tag{3.12}$$

where U is an objective function, *e.g.*, minimax function with upper and lower specifications, and $\boldsymbol{x}_f^*$ is the optimal design. The original idea behind space mapping is to determine a mapping P between the fine and coarse model inputs *i.e.*

$$\boldsymbol{x}_c = P(\boldsymbol{x}_f), \tag{3.13}$$

such that the response of the fine and coarse model match each other in the region of interest *i.e.*

$$R_c(P(\boldsymbol{x}_f)) \approx R_f(\boldsymbol{x}_f). \tag{3.14}$$

Once such a mapping is developed, estimation of $\boldsymbol{x}_f^*$ can be made using

$$\boldsymbol{x}_f \cong P^{-1}(\boldsymbol{x}_c^*), \tag{3.15}$$

without optimizing the fine model. In (3.15), $\boldsymbol{x}_c^*$ is the optimal solution in the coarse space.

3.3.2 Implicit Space Mapping (ISM)

Implicit space mapping (ISM) [42] calibrates pre-assigned mapping parameters (P), *e.g.*, the dielectric constant and loading capacitances, through parameter extraction (PE) to match the coarse and fine models' responses. The calibrated coarse model is called surrogate model (See Fig. 3.4). In standard space mapping, the mapping box and the coarse model are cascaded separately whereas is ISM the mapping is embedded within coarse model itself.

According to [42], $f^{(j)}$ is the j^{th} frequency response where the response of coarse

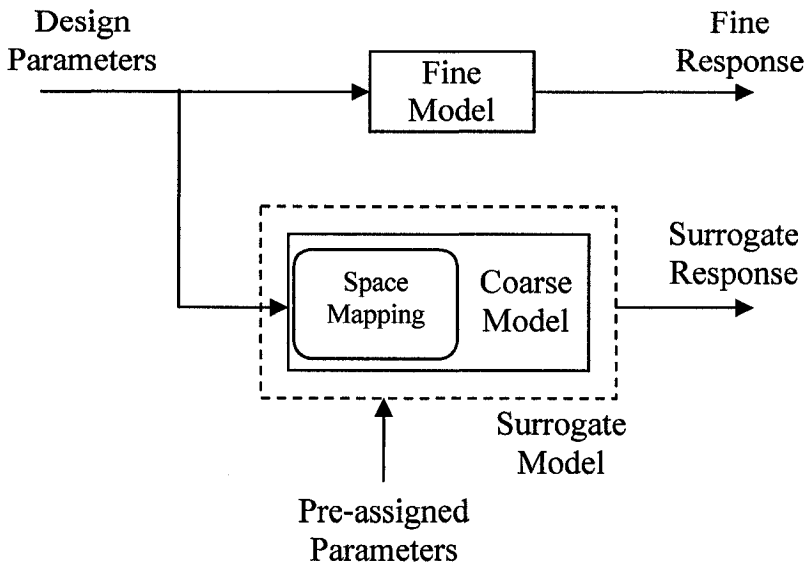

Figure 3.4: Basic concept of ISM [42].

and fine model are going to be matched and $\boldsymbol{P}^{(0)}$ is the vector containing the initial pre-assigned parameters. P^j at the j^{th} iteration is

$$P^{(j)} = \arg\min_{P} \left\| R_f(\boldsymbol{x}_c, f^{(j)}) - R_c(\boldsymbol{x}_c, f^{(j)}, P) \right\|, \quad j = 1, 2, \ldots, m. \tag{3.16}$$

After ISM modeling, the recalibrated coarse model (surrogate model) in ISM prediction is optimized in order to find the new optimized $\boldsymbol{x}_c^*$ as in (3.17)

$$\boldsymbol{x}_c^* = \arg\min_{\boldsymbol{x}_c \in X_c} U(R_c(\boldsymbol{x}_c, P^*)), \tag{3.17}$$

where X_c is the parameter space of the surrogate model. This process (ISM modeling and ISM prediction) continues until the stopping criterion is satisfied, *e.g.*, convergence is reached or the satisfactory model is met. The basic concept of ISM is illustrated in Fig. 3.4.

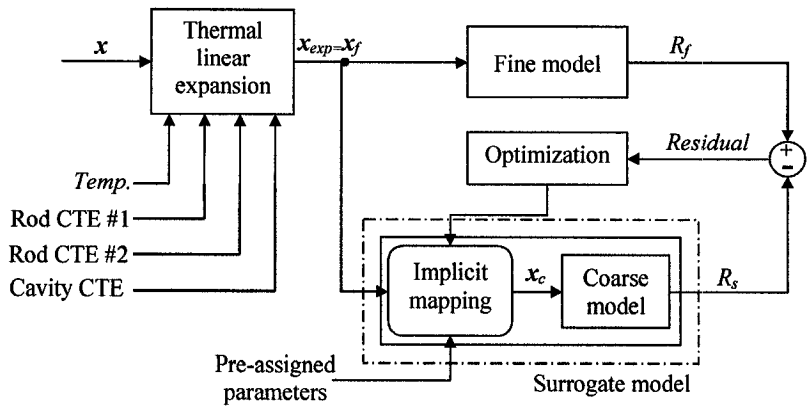

Figure 3.5: The block diagram of the ISM algorithm implementedin as part of this work.

3.4 Temperature Modeling Using ISM

A block diagram of implicit input space mapping, applied to temperature modeling of combline resonators, is shown in Fig. 3.5. In Fig. 3.5, $\boldsymbol{x}$ represents the geometry/design parameters of the combline resonator at the lab ambient temperature ($25°C$). The geometry parameters change with temperature variations. The "thermal linear expansion" block calculates the expanded geometric values ($\boldsymbol{x}_{exp}$) using equations (3.1) and (3.2). The coarse and fine model simulation are carried out and consequently the corresponding *Residus* over a frequency range of interest $f \in [f_{min}, f_{max}]$ are calculated. $R_f(\boldsymbol{x}_{exp})$ and $R_s(\boldsymbol{x}_{exp})$ represent the response of the fine and coarse model over the m frequency points of interest with expanded parameters ($\boldsymbol{x}_{exp}$). As inputs, the magnitude and phase of $Y/Z/S$ parameters matrixes are considered as possible responses for $R_f(\boldsymbol{x}_{exp}, f)$ and $R_s(\boldsymbol{x}_{exp}, f)$. The calculated *Residus* are inputted to the "optimization" box to iteratively update the pre-assigned mapping parameters.

From an implementation prospective, four steps are involved in setting up such a space-mapping-based modeling algorithm.

1. Suitable coarse and fine models are selected.

2. Suitable mapping function is selected.

3. The fine model is simulated which in this case simulation of combline resonator in *HFSS* is used.

4. The final step is parameter extraction, which is an iterative process leading to computation of mapping parameters. At the end of the fourth step, the mapping is updated and the surrogate model is derived.

A flowchart for space mapping programming is also shown in Fig. 3.6.

3.4.1 Coarse Model

Based on the equivalent circuit mentioned in section 3.2.2, the idealized coarse model for a combline resonator is a coaxial transmission line cascaded with two parallel capacitances namely C_{gap} and C_{screw} (See Fig. 3.7). This coarse model is computationally fast but it does not consider the fringing effects of loading capacitances. After setting up the coarse model, the input impedance seen through the 50Ω port of coaxial transmission line is calculated and used in parameter extraction. In this section, all the components of the coarse model are described.

The effective capacitance between the rod and the cavity C_{gap} can be calculated using parallel plate capacitor equation

$$C_{gap} = \frac{\epsilon_0 A}{r}, \tag{3.18}$$

where ϵ_0, A and r represent permittivity of the free space, area of the parallel plates, and separation between the plates respectively. The area of the parallel plates is the same as the top area of the rod structure. Screw capacitance (C_{screw}), which is caused by the penetration of the tuning screw into the rod, can be calculated using

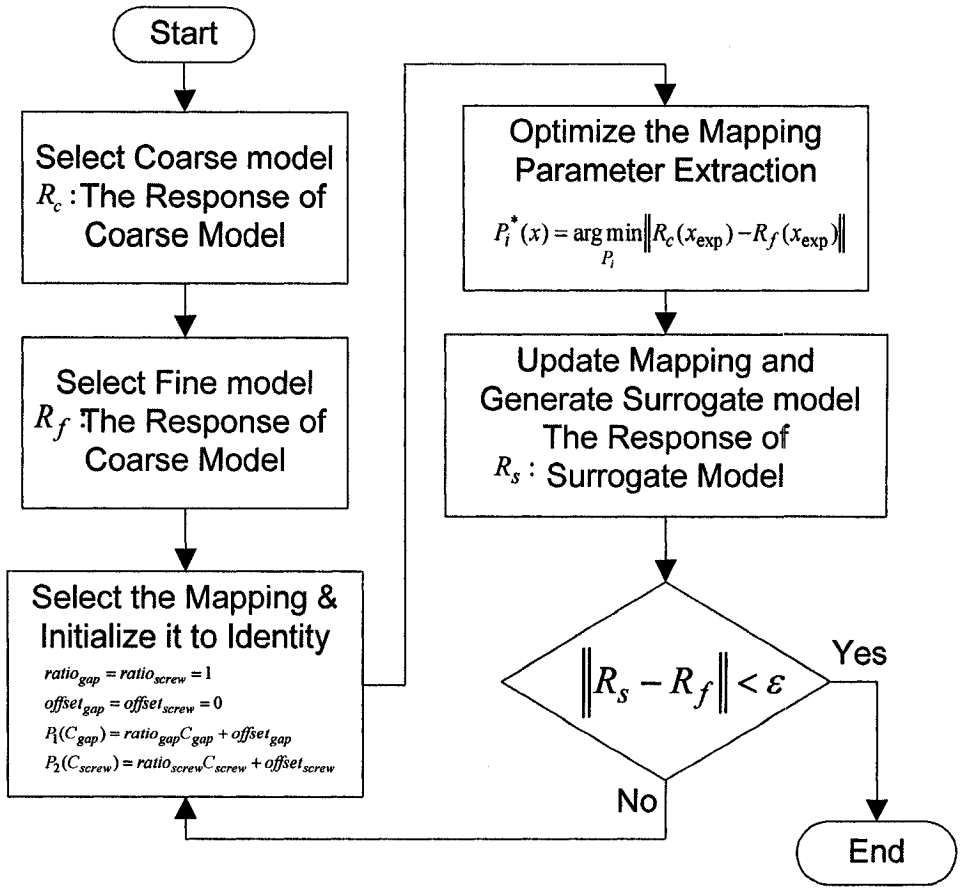

Figure 3.6: Flowchart of the space-mapping algorithm used in this chapter for temperature modeling of combline resonators.

the cylindrical capacitance equation

$$C_{screw} = \frac{2\pi s\epsilon_0}{\ln(g/h)r}v, \tag{3.19}$$

where ϵ_0, s, v, g and h denote permittivity of the free space, relative permittivity, length of screw penetration, diameter of the rod hole, and diameter of the screw respectively.

A coaxial transmission line (TL) is exploited to model the body of the cavity itself. The value of cavity diameter (a) and the rod diameter (s) are matched with the coaxial TL external diameter (D_o) and internal conductor (D_i) diameter respectively. The height of the rod (e) is also set to the length of coaxial TL (L). According to [43], the characteristic impedance for a coaxial transmission line is given as

$$Z_0 = \sqrt{\frac{\mu}{\epsilon}}\frac{\ln(a/s)}{2\pi}, \tag{3.20}$$

where s and a are the internal and external diameters of the coaxial transmission line. Once the characteristic impedance of coaxial TL and the estimated values for loading capacitances are calculated, the input impedance of coarse model is given by

$$Z_{in} = -jZ_0 \tan\frac{\omega}{3\times 10^8}(c+e) + \frac{1}{j\omega(C_{gap}+C_{screw})}, \tag{3.21}$$

where Z_0, e, and c represent characteristic impedance, height of the rod, and height of the mushroom section respectively. As mentioned earlier, since the geometry of a combline resonator changes with temperature, the absolute geometrical values are replaced by temperature-dependent symbolic expressions as shown in Fig. 3.7.

3.4.2 Fine Model

In this work, EM simulations of combline resonators based on Ansoft's *HFSS* are considered as the fine model responses. EM data from *HFSS* consisting of S-parameters

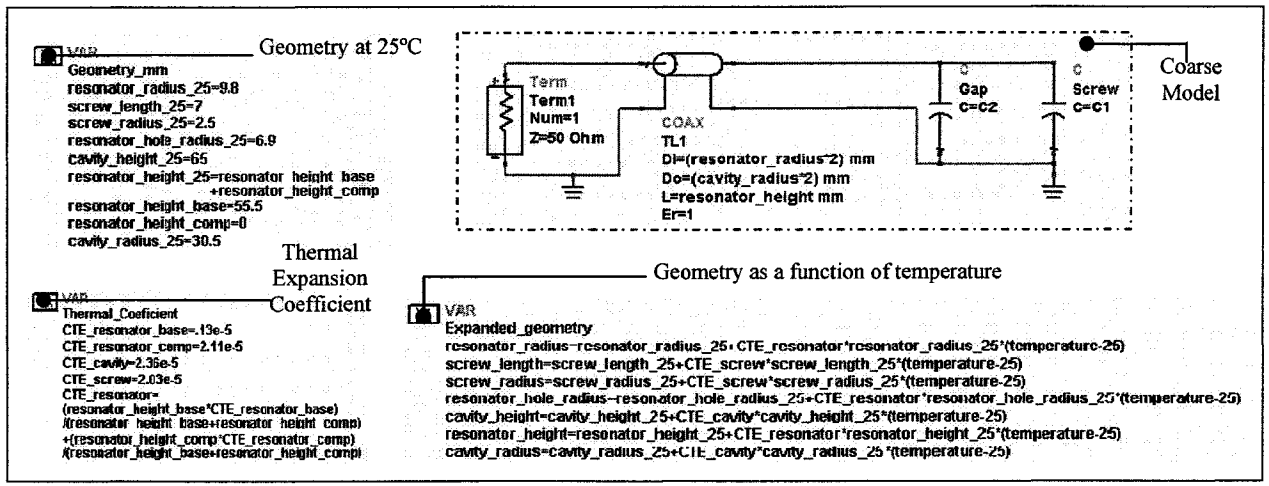

Figure 3.7: Representation of the coarse model as a function of temperature and ϑ in *ADS*.

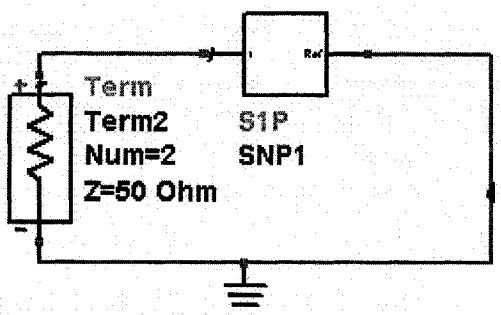

Figure 3.8: S1P representation in *ADS*.

versus frequency is obtained in touchstone format. An S-parameter file, namely SnP in Agilent's *ADS*, can import such data. In SnP, n stands for the number of ports. For example, Fig. 3.8 depicts a one-port S-parameter file component (S1P). It is to be noted that S-parameters can then be converted into Z-parameters by library functions of *ADS* or *MATLAB*.

There are two key factors to achieving fast and accurate fine model simulations in *HFSS i.e.* assigning proper excitation and setting proper boundary conditions. First, some aspects of excitation are discussed. In practice, combline resonators are usually excited by a SMA Female Chassis Mount Receptable connector screwed from the side to the body of cavity (See. Fig. 3.9). Since in the implemented space mapping algorithm, the coarse model is excited as a coaxial TL, the implemented excitation in *HFSS* should model the same type of behavior. As such the wave port is located on the bottom face of the combline resonator (See. Fig. 3.10) and all the other wave port parameters are set to their default values to excite the first dominant mode at the specified centre frequency.

Second, some aspects of boundary conditions are discussed. Assigning "Perfect E" boundary condition is necessary to model the perfect conductor effects on the inner cavity wall (See Fig. 3.11). Alternatively, in order to simplify the simulation using symmetric structure of combline resonator, there are other guidelines to de-

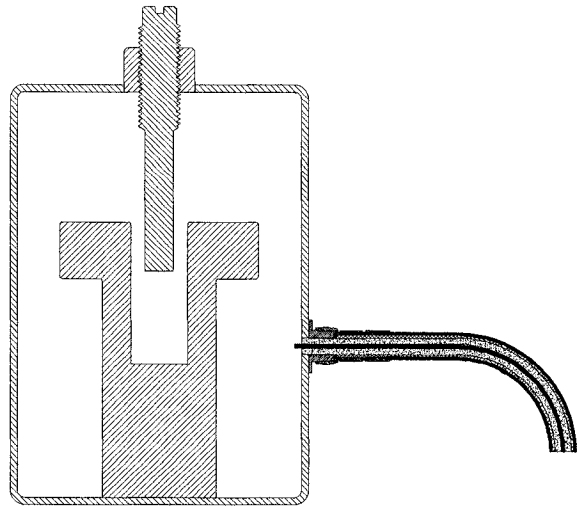

Figure 3.9: Combline resonators excited by a SMA Female Chassis Mount Receptacle connector screwed from the side to the body of cavity.

cide which type of symmetry boundary conditions to use. These symmetry boundary conditions allows for the simulation of a small portion of a combline resonator which results in less CPU and memory resources. If the symmetry is such that the E-field is normal to the symmetry plane, a "perfect E" should be exploited. In other cases where the symmetry plane is such that the E-field is tangential to the symmetry plane, a "perfect H" is assigned to the symmetry plane. In the case of a combline resonator a "perfect H" boundary condition is assigned to the symmetry plane (See Fig. 3.12).

3.4.3 Mapping Function

The capacitance values calculated using equations (3.18) and (3.19) do not account for nonlinear fringing effects *e.g.* fringing that depends on the geometry of the rod. As such, it is necessary to adjust these approximate values to accurate ones. This is

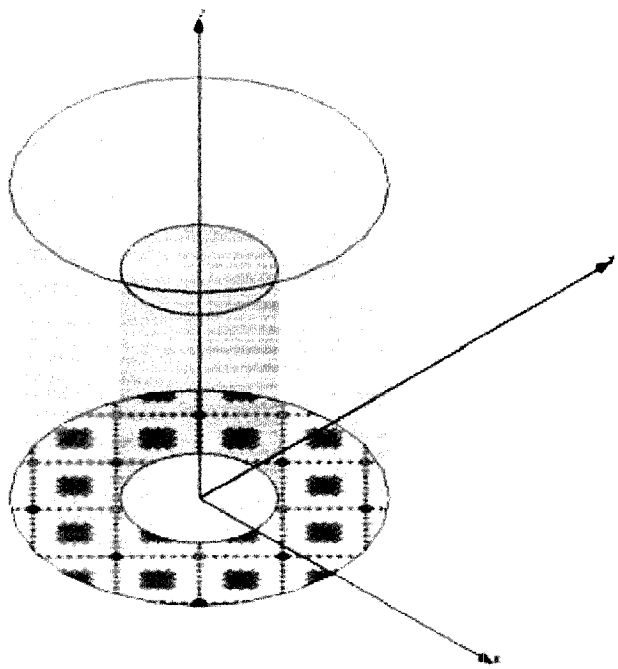

Figure 3.10: Excited face (highlighted area).

accomplished using linear mapping given by

$$C_{gap+fringing} = ratio_{gap} \times C_{gap} + offset_{gap} \tag{3.22}$$

and

$$C_{screw+fringing} = ratio_{screw} \times C_{screw} + offset_{screw}, \tag{3.23}$$

where *ratios* and *offsets* are mapping parameters. Implementation details are shown in Fig. 3.13(a).

3.4.4 Parameter Extraction

As mentioned earlier, responses of coarse and fine models are matched through a parameter-extraction process. More specifically, $ratio_{gap}$, $ratio_{screw}$, $offset_{gap}$ and

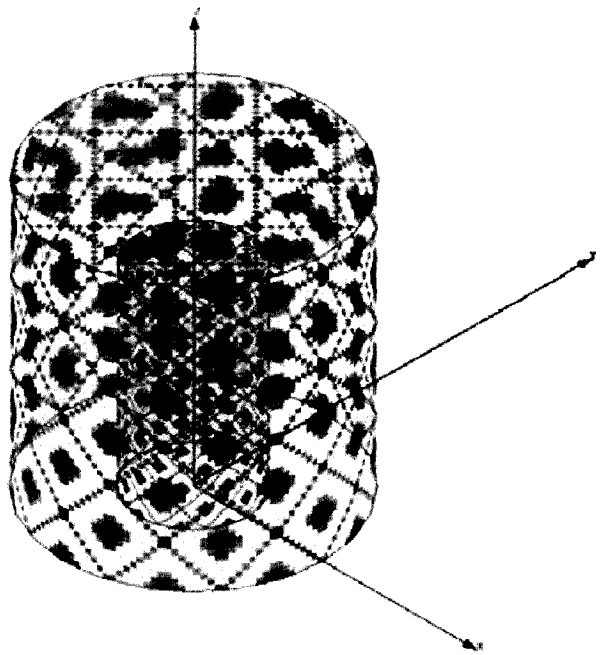

Figure 3.11: The highlighted areas show Perfect E boundary condition assignment to model the perfect conductor on inner cavity wall.

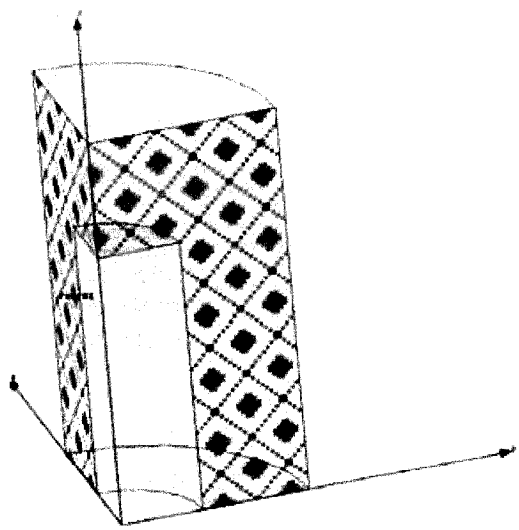

Figure 3.12: The highlighted area show the area which has been assigned by proper symmetry boundary (perfect H).

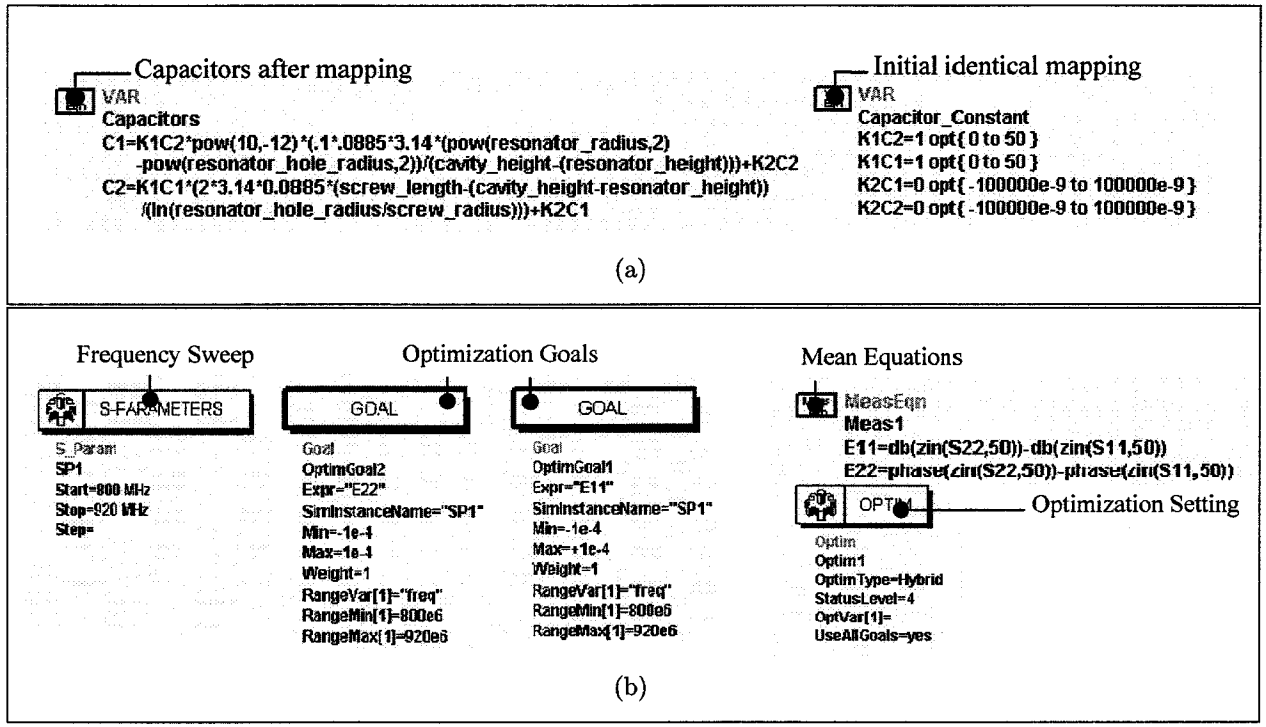

Figure 3.13: (a) Implementation of the proposed linear mapping in ADS taking into account the fringing effects (b) Implementation of the optimization procedure is ADS leading to parameter extraction.

$offset_{screw}$ in (3.22) and (3.23) are iteratively adjusted based on full-wave EM simulations from the fine model *i.e.* Ansoft's *HFSS*. To implement this step, an optimization framework shown in Fig. 3.13(b) has been setup in *ADS*. The goal for such optimization process is to accurately match both magnitude and phase of Z_{in} computed using coarse and fine models. Hybrid optimization option in *ADS* is employed. The optimization problem can be formulated as

$$\boldsymbol{P}^* = \arg\min_{\boldsymbol{P}} \left\| R_f(\boldsymbol{x}_{exp}, f) - R_c(\boldsymbol{x}_{exp}, f) \right\|, \tag{3.24}$$

where $\boldsymbol{P}$ is

$$\boldsymbol{P} = \begin{bmatrix} P_1 \\ P_2 \end{bmatrix} = \begin{bmatrix} ratio_{gap} \\ offset_{gap} \\ ratio_{screw} \\ offset_{screw} \end{bmatrix}. \tag{3.25}$$

3.5 Numerical Results

For the purpose of illustration, a combline resonator with mushroom structure is considered. EM simulations have been performed using *HFSS* and resulting S-parameter data is loaded into *ADS via* an S1P file. Fig. 3.14 shows the matching of Z_{in} from the coarse model (after parameter extraction and coarse model update) and the fine model. The combline resonator is simulated for two different rod materials: stainless steel and invar. The results show a $\pm 2 ppm/°C$ error, which is satisfactory in terms of model accuracy. Table 3.2 shows a comparison of the results from both simulations and measurements.

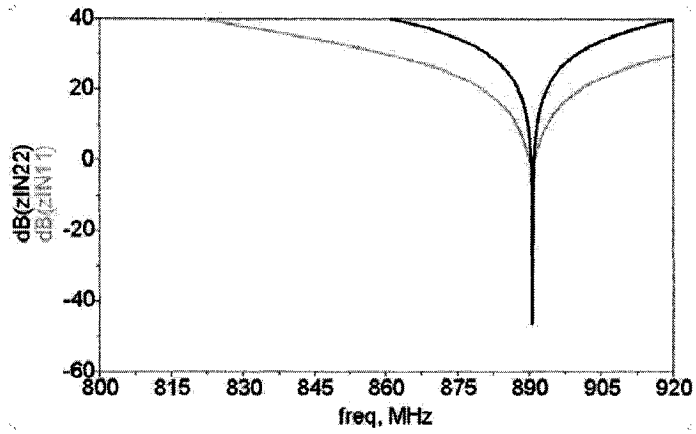

(a)

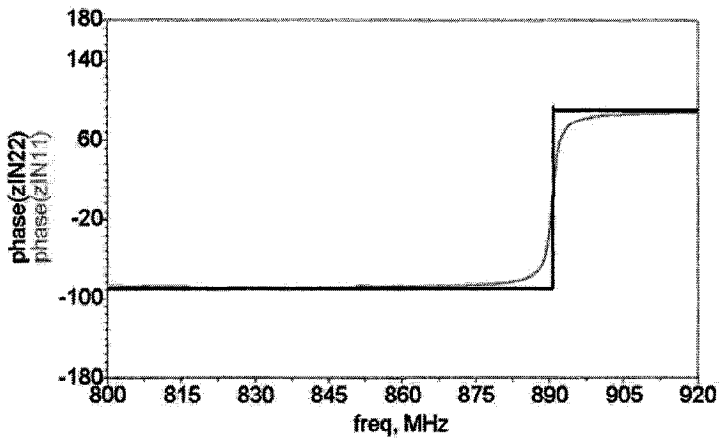

(b)

Figure 3.14: (a) Magnitude of the input impedance computed using the coarse (zIN11) and the fine (zIN22) models (b) Phase of the input impedance computed using the coarse (zIN11) and the fine (zIN22) models.

Table 3.1: Geometry of the combline resonator.

Geometry	mm
Cavity Diameter (a)	61
Cavity Height (b)	65
Resonator Mushroom Height (c)	3
Resonator Mushroom Diameter (d)	34
Resonator Base Height (e)	52.5
Resonator Base Diameter (s)	19.06
Resonator Hole Diameter (g)	13.8
Screw Diameter (h)	5
Screw Length (v)	15

Table 3.2: Comparison of numerical results from simulations and measurements.

	CTE Cavity	Aluminum 6061 (23.6 $ppm/°C$)
	CTE Screw	Brass (20.3 $ppm/°C$)
Case 1	CTE Resonator	SS (9.9 $ppm/°C$)
	Temperature Drift (Simulated)	-6.714 $ppm/°C$
	Temperature Drift (Measured)	-4.93 $ppm/°C$
Case 2	CTE Resonator	Invar (1.3$ppm/°C$)
	Temperature Drift (Simulated)	+1.856 $ppm/°C$
	Temperature Drift (Measured)	+1.82 $ppm/°C$

3.6 Summary

A CAD model based on space-mapping has been proposed. Using the systematic steps of this methodology, temperature behavior of a variety of combline resonator structures can be modeled. This modeling algorithm is suitable for compensation designs where the type of material to be used should be determined. The resulting models are accurate and fast around the expansion point and hence can be of practical significance in RF/microwave filter design/optimization.

Chapter 4

FDTD-Based Modeling of Resonant Frequency for Combline Resonators

4.1 Introduction

Low cost and easy manufacturing process have made combline resonators attractive for RF/microwave systems such as filters and oscillators. A major challenge in filter design using combline resonators is to achieve a frequency response which is independent of temperature. This aspect becomes even more critical in the design of narrow band filters. To be able to design filters with robust frequency response, one should be able to accurately estimate frequency drift due to temperature.

Numerical solutions to Maxwell's equations *e.g.* finite element (FEM) [45] and and finite difference time-domain (FDTD) [46] are full-wave methods used in modeling the temperature behavior of combline resonators. One of the difficulties in FEM based methods is potential non-convergence owing to the large scale eigenvalues problem with tens to hundreds of thousands degree of freedom [44]. The other problem of FEM is that simulating for a broad frequency range becomes prohibitively

time-consuming. Alternatively in FDTD-based methods, the 3D grid generated to solve for time-domain electromagnetic field pattern, is prohibitively large and uses a considerable portion of memory resources. Besides, in order to achieve a frequency response with a reasonable accuracy, FDTD based methods require lot of CPU time.

One of the recent works in temperature modeling of combline resonators has exploited the space mapping technique [39]. Although space mapping yields fast and accurate models for combline resonators with arbitrary structures, temperature compensation methods using space mapping models are limited to material optimization *i.e.* the type of material to be used in the structure of a combline resonator. Although material based compensation methods remain attractive, there is a growing need for new structures that intrinsically possess temperature-independent behavior. In situations involving generalized structures, application of FDTD and FEM becomes critical.

Mittra [46] proposed a fast FDTD method for cylindrically symmetric structures where the 3D conventional Yee cell [47] structure is mapped into a 2D cell structure. Day [44] integrated FDTD algorithm with rational functions (Padé expression) to avoid simulation for large time intervals and yet maintain an acceptable accuracy.

In this chapter, an efficient FDTD method is combined with Padé expression to model the cut-off frequency drift of the dominant mode due to small geometry variations. Such small geometry variations can indirectly represent the frequency drift as a result of temperature. In other word, in this work, the temperature is not directly involved in the FDTD formulation of Maxwell's equation but considered in the geometry. In this direction, the work of [46] and [44] are integrated to generate fast and efficient temperature models of combline resonators. The integrated method efficiently works for temperature modeling and uses less CPU and memory resources in comparison to other numerical methods such as FEM. The Q parameters can also be extracted using the techniques represented in this chapter. In the context of filter design, a higher Q will results in a better signal to noise ratio. Through examples, it

is shown that FDTD algorithms integrated with Padé expressions accurately model slight geometry changes (*i.e.* frequency drift) due to temperature.

4.2 FDTD Algorithm for Rotationally Symmetrical Structures

4.2.1 Angular Variation Factoring

In [46], a simplified two dimensional FDTD algorithm for rotationally symmetric structures is introduced. This simplified FDTD algorithm assumes that the angular variation of electromagnetic fields has either a $\sin(m\phi)$ or $\cos(m\phi)$ variation, and hence this angular behavior can be factored out from Maxwell's equations. Using generalized matrix operators [48] in the cylindrical coordinate system, the Maxwell's curl equations can be represented as

$$\begin{bmatrix} 0 & -\partial_z & \pm m/r \\ \partial_z & 0 & \partial_r \\ \mp m/r & (\partial r_r/r) & 0 \end{bmatrix} \begin{bmatrix} E_r \\ E_\phi \\ E_z \end{bmatrix} = - \begin{bmatrix} (\mu_0\mu_r\partial_t + \sigma_{mr})H_r \\ (\mu_0\mu_\phi\partial_t + \sigma_{m\phi})H_\phi \\ (\mu_0\mu_z\partial_t + \sigma_{mz})H_z \end{bmatrix} \tag{4.1}$$

and

$$\begin{bmatrix} 0 & -\partial_z & \mp m/r \\ \partial_z & 0 & \partial_r \\ \pm m/r & (\partial r_r/r) & 0 \end{bmatrix} \begin{bmatrix} H_r \\ H_\phi \\ H_z \end{bmatrix} = - \begin{bmatrix} (\epsilon_0\epsilon_r\partial_t + \sigma_{er})E_r \\ (\epsilon_0\epsilon_\phi\partial_t + \sigma_{e\phi})E_\phi \\ (\epsilon_0\epsilon_z\partial_t + \sigma_{ez})E_z \end{bmatrix}, \tag{4.2}$$

where ∂_α represents a partial derivative *w.r.t.* one of r, z or t. In (4.1) and (4.2), μ, ϵ, σ_m and σ_e represent permeability, permittivity, magnetic and electric conductivity respectively. In the following σ_m and σ_e are set to zero for the sake of simplicity.

4.2.2 The Mapped 2D Lattice

In view of equations (4.1) and (4.2), the fields at any arbitrary $\phi = \phi_0$ plane can be readily related to their corresponding value in the reference ϕ plane. *i.e.* $\phi = 0$. This helps reduce the original Yee algorithm in 3D to an equivalent 2D one, at the $\phi = 0$. The work in [46] starts with the 3D Yee-Cell in cylindrical coordinates and projects it into $r - z$ plane resulting in the 2D finite difference lattice. A unit cell of new projected cell is shown in Fig. 1. Such a unit cell possesses all six electric and magnetic components along cylindrical coordinates. This 2D lattice is different from the conventional 3D case in the following two ways:

1. (E_z, H_r) and (E_r, H_z) share the same geometrical locations.

2. E_ϕ is located at the four corners of the cell. However, as in the conventional Yee lattice, H_ϕ still resides at the centre of the face.

4.2.3 FDTD Formulation of the 2D Lattice

According to [46], after disceretizing the two curl equations (4.1) and (4.2) in the 2D cell in Fig. 4.1, the discretizied equations are given by

$$\begin{aligned} E_r^{n+1}(i,j) =& \frac{\left(1 - \frac{\sigma_r \Delta t}{2\epsilon_0 \epsilon_r}\right)}{\left(1 + \frac{\sigma_r \Delta t}{2\epsilon_0 \epsilon_r}\right)} E_r^n(i,j) - \frac{\frac{m\Delta t}{\epsilon_0 \epsilon_r}}{\left(1 + \frac{\sigma_r \Delta t}{2\epsilon_0 \epsilon_r}\right)} \frac{H_z^{n+1/2}(i,j)}{r_{i+1/2}} \\ & - \frac{\frac{\Delta t}{\epsilon_0 \epsilon_r}}{\left(1 + \frac{\sigma_r \Delta t}{2\epsilon_0 \epsilon_r}\right)} \cdot \left[\frac{H_\phi^{n+1/2}(i,j) - H_\phi^{n+1/2}(i,j-1)}{\Delta z} \right], \end{aligned} \tag{4.3}$$

$$E_{\phi}^{n+1}(i,j) = \frac{\left(1-\frac{\sigma_{\phi}\Delta t}{2\epsilon_0\epsilon_{\phi}}\right)}{\left(1+\frac{\sigma_{\phi}\Delta t}{2\epsilon_0\epsilon_{\phi}}\right)} E_{\phi}^{n}(i,j) + \frac{\frac{\Delta t}{\epsilon_0\epsilon_{\phi}}}{\left(1+\frac{\sigma_{\phi}\Delta t}{2\epsilon_0\epsilon_{\phi}}\right)} \cdot \left[\frac{H_r^{n+1/2}(i,j) - H_r^{n+1/2}(i,j-1)}{\Delta z}\right] - \frac{\frac{\Delta t}{\epsilon_0\epsilon_{\phi}}}{\left(1+\frac{\sigma_{\phi}\Delta t}{2\epsilon_0\epsilon_{\phi}}\right)} \cdot \left[\frac{H_z^{n+1/2}(i,j) - H_z^{n+1/2}(i-1,j)}{\Delta r}\right], \tag{4.4}$$

$$E_z^{n+1}(i,j) = \frac{\left(1-\frac{\sigma_z\Delta t}{2\epsilon_0\epsilon_z}\right)}{\left(1+\frac{\sigma_z\Delta t}{2\epsilon_0\epsilon_z}\right)} E_z^{n}(i,j) + \frac{\frac{m\Delta t}{\epsilon_0\epsilon_z}}{\left(1+\frac{\sigma_z\Delta t}{2\epsilon_0\epsilon_z}\right)} \cdot \frac{H_r^{n+1/2}(i,j)}{r_i} + \frac{\frac{\Delta t}{\epsilon_0\epsilon_z}}{\left(1+\frac{\sigma_z\Delta t}{2\epsilon_0\epsilon_z}\right)} \cdot \left[\frac{r_{i+1/2}H_{\phi}^{n+1/2}(i,j) - r_{i-1/2}H_{\phi}^{n+1/2}(i-1,j)}{\Delta r}\right], \tag{4.5}$$

$$H_r^{n+1/2}(i,j) = H_r^{n-1/2}(i,j) - \frac{m\Delta t}{\mu_0\mu_r r_i} E_z^{n}(i,j) + \frac{\Delta t}{\mu_0\mu_r}\left[\frac{E_{\phi}^{n}(i,j+1) - E_{\phi}^{n}(i,j)}{\Delta z}\right], \tag{4.6}$$

$$H_{\phi}^{n+1/2}(i,j) = H_{\phi}^{n-1/2}(i,j) - \frac{\Delta t}{\mu_0\mu_{\phi}} \cdot \left[\frac{E_r^{n}(i,j+1) - E_r^{n}(i,j)}{\Delta z} - \frac{E_z^{n}(i+1,j) - E_z^{n}(i,j)}{\Delta r}\right], \tag{4.7}$$

and

$$H_z^{n+1/2}(i,j) = H_z^{n-1/2}(i,j) + \frac{m\Delta t}{\mu_0\mu_z r_{i+1/2}} E_r^{n}(i,j) - \frac{\Delta t}{\mu_0\mu_z} \cdot \left[\frac{r_{i+1}E_{\phi}^{n}(i+1,j) - r_i E_{\phi}^{n}(i,j)}{r_{i+1/2}\Delta r}\right] \tag{4.8}$$

where $r_i = \Delta r(i-1/2)$ and $r_{1/2} = r_0 = 0$. The above equations are suitable for the time domain iteration once the problem of singularities at $r = 0$ for E_r, E_z and H_z has been addressed.

4.2.4 Handling Singularities at $r = 0$

On the natural boundary $r = 0$ there exists a total of three components E_r, H_ϕ and H_z [46]. However, as seen of equations (4.4) and (4.5), only the components tangential to this boundary, *i.e.* H_ϕ and H_z, are needed to update the adjacent E_ϕ and E_z fields internal to the mesh. In order to compute E_z at $i = 1$, H_ϕ at $i = 0$ is to be multiplied by a factor $r_{i-1/2} = 0$. As such, computation of H_ϕ at $r = 0$ is not required. H_z is the other element that must be defined on the natural boundary. It may be noted from the E_ϕ updating equation (4.4) at $i = 1$, the value of H_z at $i = 0$ is required. In summary, only H_z is needed at the boundary $i = 0$ to update all the relevant fields. Since in the dominant mode under consideration ($TE_{z(011)}$) the angular variation along ϕ is zero, m in all of the updating equations should be set to zero. Hence, H_z is required to be evaluated at $r = 0$ for $m = 0$. The integral form of Maxwell's equations in the time-domain is

$$\oint_{\Delta C} \overline{E}.\overline{dl} = -\iint_{\Delta S} \mu \frac{\partial \overline{H}}{\partial t}.d\overline{S}, \tag{4.9}$$

where ΔS and ΔC are the finite difference area and integral paths defined in Fig. 4.2. From (4.5), the discretized time update equation for H_z at $r = 0$ and $m = 0$ is given by

$$H_z|_{o,j}^{n+1/2} = H_z|_{o,j}^{n-1/2} - \frac{4\Delta t}{\mu_0 \mu_z \Delta_r} E_\phi|_{1,j}^{n}. \tag{4.10}$$

4.3 Dispersion

In the time-domian simulation, the maximum time-step for stability [50] follows from the requirement

$$c\Delta t \leq \left[\frac{1}{(\Delta r)^2} + \frac{1}{(\Delta \phi)^2} + \frac{1}{(\Delta z)^2}\right]^{-1/2} \tag{4.11}$$

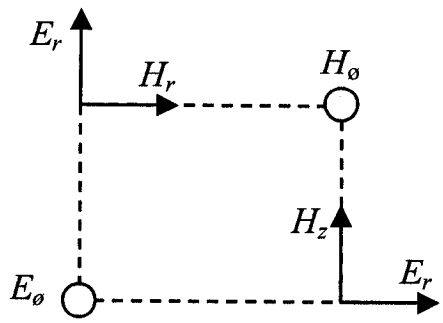

Figure 4.1: The projected 2D cell.

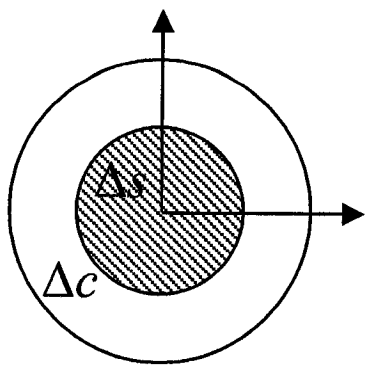

Figure 4.2: Integral path to evaluate H_z at $r = 0$.

where c is the speed of light. Since the original 3D cell is projected into an equivalent 2D cell, $1/(\Delta\phi)^2$ factor is unavailable. In the absence of value for $1/(\Delta\phi)^2$, Δt is determined by a trial-and-error. Equation (4.11) is simplified to

$$c\Delta t \leq k_c \left[\frac{1}{(\Delta r)^2} + \frac{1}{(\Delta z)^2}\right]^{-1/2}. \tag{4.12}$$

In (4.12), the regular dispersion equation is simply multiplied by a factor of k_c to compensate for the absence of undetermined $1/(\Delta\phi)^2$ factor.

4.4 Excitation

In order to achieve the initial field transitions as well as the final standing waves, the cavity must be excited with a band width limited signal. The bandwidth of the excitation signal should be in the frequency range in which the cavity is being analyzed. As suggested in [46], the Blackman-Harris (BH) window excitation function is used in this work [49]. This window function provides a smoother transition of the excitation function. There two tunable variables for BH : t_c which indicates the time position for the centre of the window function and N_{half} which represents the half width of the BH window function. In practice, smaller values of N_{half} result in a broader frequency range. BH excitation is designed in a manner such that it is turned on only during a designed time interval $t_n \in [t_c - N_{half}, t_c + N_{half}]$. BH excitation in the "on" period is shown in given by

$$\chi(t_n) = 0.35 + 0.48\cos(\frac{\pi(t_n - t_c)}{N_{half}}) + 0.14\cos(\frac{2\pi(t_n - t_c)}{N_{half}}) + 0.01\cos(\frac{3\pi(t_n - t_c)}{N_{half}}). \tag{4.13}$$

In the context of temperature modeling, designers are interested to analyze the behavior of a cavity within a narrow frequency bandwidth around the centre frequency. As such, the BH excitation parameters (t_c and N_{half}) should be adjusted such that the

excitation signal has a narrow band frequency spectrum at around frequency range of interest.

4.5 Padé Expression

The afore-mentioned FDTD method results in a time-domain response. This time-domain response is transferred to frequency-domain by performing a Fast Fourier Transformation (FFT). The FFT, however, requires a large number of time samples to calculate the resonant frequency with reasonable accuracy and resolution, and this translates to a relatively long computation time. To overcome this limitation, Padé expression is used in conjunction with the FFT to approximate the coarse frequency response in a two step process [44]. First, the FFT is applied on the time-domain data to obtain the frequency response. Second, frequency response is further processed using Padé expression leading to improved accuracy. More specifically, the second step involves fitting the frequency response into a rational function *i.e.*

$$s(\omega) \approx \sum_{n} \frac{C_n}{\omega - \omega_n}. \tag{4.14}$$

by adjusting the unknown coefficients and poles *i.e.* C_n and ω_n in equation (4.14).

Once such poles (ω_n) are identified, resonant frequencies can be accurately determined. In Fig. 4.3, it is evident that the conventional FFT is unable to resolve two resonance frequencies when they are close to each other. However, the new method can easily extract the correct resonant frequencies.

4.6 Numerical Results

An in-house FDTD-based program is developed by integrating the rotationally symmetric FDTD algorithm [46] and Padé expression [44]. Temperature behavior of two

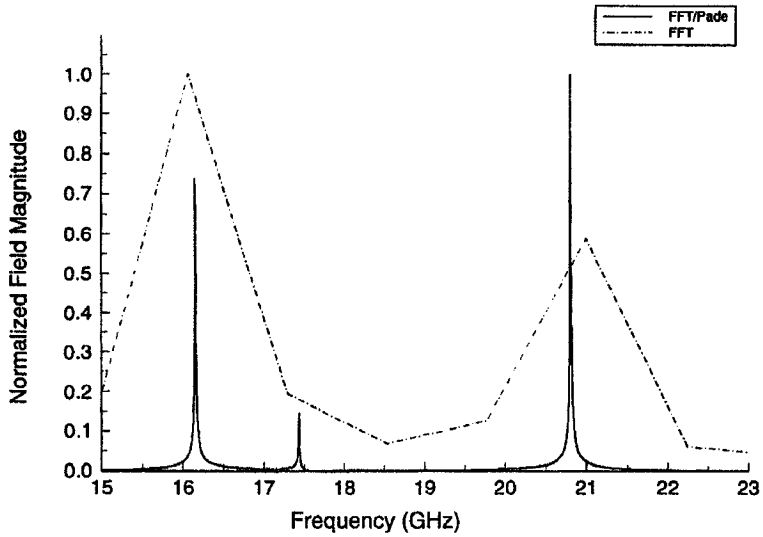

Figure 4.3: Normalized frequency response of rectangular cavity with conventional FFT and FFT/Padé technique [44].

cylindrical cavities in Fig. 4.4 is investigated. Responses generated using analytical solutions, in-house FDTD program and *HFSS* are compared in Table 4.2. In both examples, the cut-off frequency of dominant TE_{011} mode is considered.

4.6.1 Simple Combline Resonator

A simple cylindrical cavity (an unperturbed combline resonator) is considered. To evaluate analytical solutions to the resonant frequency of cylindrical cavities are available in the form of *Bessel* functions. Simple structures, such as one in this example, are commonly used to validate in-house programs. A cross-section of the empty cylindrical cavity and its dimensions are shown in Fig. 4.4(a). Analytical resonant frequencies [43] for two temperatures for $TE_{z(011)}$ which is the dominant mode are listed in Table 4.2. Simulation in *HFSS* is carried out and after generating 10907 tetrahedra, a satisfactory convergence is observed (max. $\Delta f < 0.001$). Finally, the in-house FDTD program is applied. The structure has been discretized by a 50×100

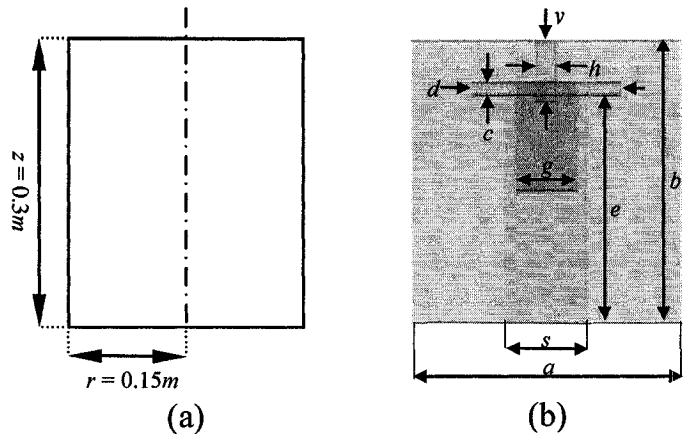

Figure 4.4: (a) Simple cylindrical cavity (b) Mushroom combline resonator.

Table 4.1: Geometry of the combline mushroom resonator.

Geometry	mm
Cavity Diameter (a)	61
Cavity Height (b)	65
Resonator Mushroom Height (c)	3
Resonator Mushroom Diameter (d)	34
Resonator Base Height (e)	52.5
Resonator Base Diameter (s)	19.06
Resonator Hole Diameter (g)	13.8
Screw Diameter (h)	5
Screw Length (v)	15

cells along r and z respectively. The time stepping (Δt) for the FDTD algorithm is set to 4.9532×10^{-12} sec which is ten times smaller than the shortest wavelength under consideration ($\lambda = 0.3m, f = 3\text{GHz}$). t_c and N_{Half} for Blackman-Harris excitation are set to 3.7501×10^{-9} sec and 2.8068×10^{-9} sec respectively. In order to avoid a DC value in excitation, the Gaussian pulse has been modulated with a 1.1GHz carrier. In Fig. 4.5(a), a frequency spectrum of the field component E is illustrated at cell [20,60] for the dominant $TE_{z(011)}$ mode. In Fig. 4.6.(a) the amplitude of electrical filed is shown and it can be easily concluded that the excited mode is $TE_{z(011)}$. Re-

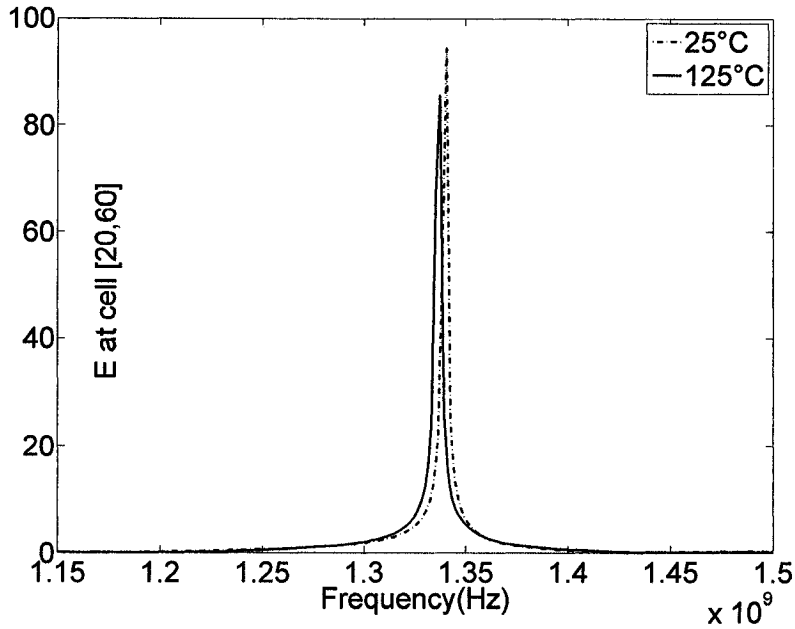

(a)

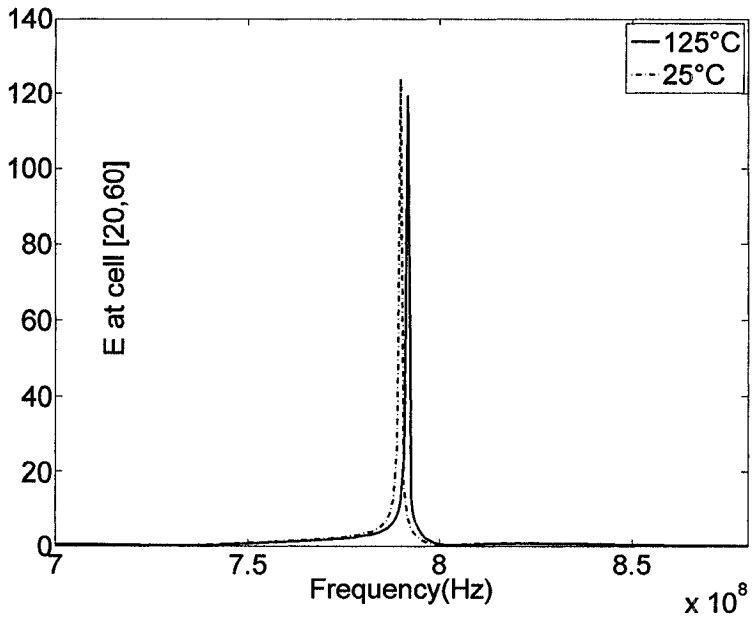

(b)

Figure 4.5: (a) The cut off frequency of dominant $TE_{z(001)}$ mode for simple cavity (b)The cut off frequency of dominant $TE_{z(001)}$ mode for mushroom Cavity.

sults show that the in-house FDTD program converges much faster that Eigen-Mode solution in *HFSS* as shown in Table 4.2.

4.6.2 Mushroom Combline Resonator

A combline resonator with mushroom rod structure is considered. Analytical solutions to the resonant frequency of perturbed combline resonators are not available. Hence corresponding entries in Table 4.2 are left blank. The cross section of the mushroom cavity and its geometric parameters are shown in Fig. 4.4.(b) and Table 4.1 respectively.

Simulation in *HFSS* is performed and after generating 7779 tethrahedras a satisfactory convergence is met (max. $\Delta f < 0.001$). The in-house FDTD program is applied. The structure has been discretized by a 50×100 cells along r and z respectively. The time stepping (Δt) for the FDTD algorithm is set to 1.4088×10^{-9} sec which is ten times smaller than the shortest wavelength under consideration ($\lambda = 0.3m, f = 3\text{GHz}$). t_c and N_{Half} for Blackman-Harris excitation are set to 1.4088×10^{-9} sec and 5.9694×10^{-10} sec respectively. In order to avoid a DC term in our excitation, the Gaussian pulse has been modulated with a 1.3GHz carrier.

In Fig. 4.5.(b), a frequency spectrum of the field component E at cell [20,60] is illustrated for the dominant $TE_{z(011)}$ mode. In Fig. 4.6.(b) the amplitude of electrical filed is shown and it can be easily concluded that we have exactly excited $TE_{z(011)}$. Results show that the in-house program converges much faster than eigen-mode solution in *HFSS* as the results in Table 4.2.

4.7 Summary

FDTD method for solving Maxwell's equations in rotationally symmetric geometries has been integrated with Padé expression to generate a temperature model of combline resonators. Through practical examples, it has been shown that a FDTD algorithm

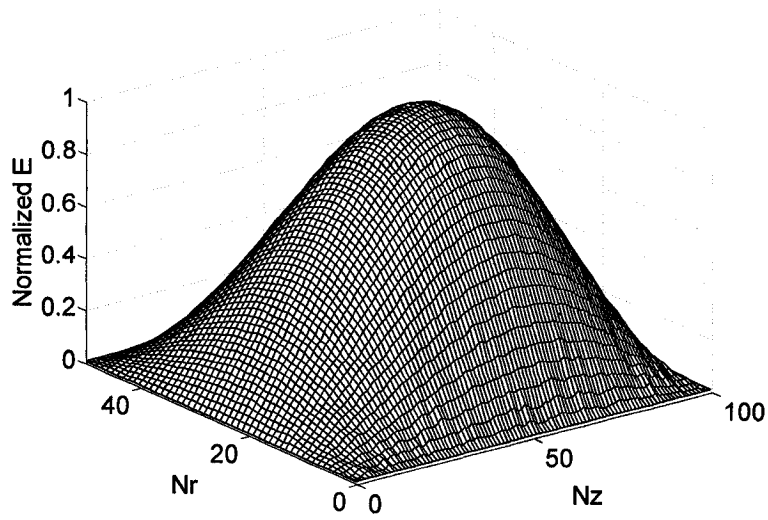

(a)

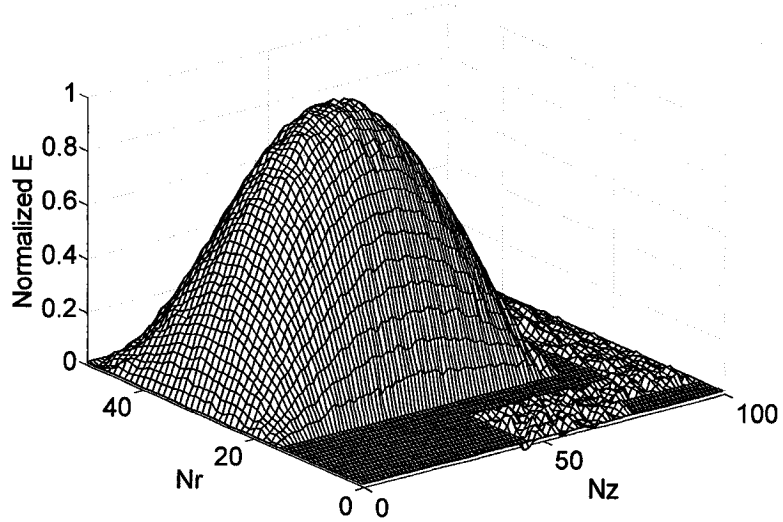

(b)

Figure 4.6: (a) Normalized electric field for simple cavity (b) Normalized electric field for mushroom cavity.

with a uniform grid distribution is fully capable of modeling temperature behavior of combline resonators. The advantage of this work over other numerical solutions is the required memory and CPU resources. This modeling technique can hence be applied to temperature compensation methods where a geometry optimization required.

Table 4.2: Numerical results.

	Simple Cavity		Mushroom Cavity	
Temperature	25°C	125°C	25°C	125°C
Analytical Resonant Frequency	1.31818 GHz	1.31473 GHz	NA	NA
Resonant Frequency (HFSS)	1.2583 GHz	1.2552 GHz	0.77187 GHz	0.77358 GHz
Resonant Frequency (in-house FDTD program)	1.34056 GHz	1.33722 GHz	0.79008 GHz	0.79194 GHz
Frequency Drift using HFSS	-3.1MHz -0.031$ppm/°C$		+1.71MHz +0.017$ppm/°C$	
Frequency Drift using in-house FDTD program	-3.3MHz -0.034$ppm/°C$		+1.86MHz +0.018$ppm/°C$	
Required time (HFSS)	415 sec		359 sec	
Required time (in-house FDTD program)	136 sec		75 sec	
CTE Cavity	Aluminum(6061) 23.6$ppm/°C$			
CTE Screw	NA		Brass 20.3$ppm/°C$	
CTE Rod	NA		Invar 1.3$ppm/°C$	

Chapter 5

Conclusions

5.1 Overall Summary

In this thesis, enhanced frequency sampling algorithms for automatic development of EM-based RF/microwave rational interpolants have been proposed for both single and multidimensional problems. Starting with a minimal number of EM data and lowest-order rational functions, these algorithms iteratively build surrogate models, which satisfy user-specified model accuracies. Using the new proposed dynamic grid, the algorithms use relatively fewer samples than the standard algorithms to achieve similar model accuracies, and are hence suitable for recursive optimization algorithm. Illustration examples show that in contrast to the standard algorithms, the proposed algorithms avoid over-sampling around critical regions and significantly reduce the number EM samples and yet maintain the user-defined accuracy.

In this thesis, a new CAD modeling technique based on space-mapping has been proposed. Using the systematic steps of this technique, temperature behavior of a variety of combline resonator structures can be modeled. This modeling technique is suitable for compensator design where the type of material to be used should be determined. The resulting models are accurate and fast around the expansion point and hence can be of practical significance in RF/microwave filter design/optimization.

In this thesis, FDTD method for solving Maxwell's equations in rotationally symmetric geometries has been integrated with Padé approximation to generate a temperature model of combline resonators. Through practical examples, it has been shown that a FDTD algorithm with a uniform grid distribution is fully capable of modeling temperature behavior of combline resonators. The advantage of this work over other numerical solutions is the required memory and CPU resources. This modeling technique can hence be applied to temperature compensation methods where a geometry optimization is required.

All the discussed EM-based modeling techniques in this thesis have a potential to accelerate the convergence of algorithms employed in RF and microwave design and optimization. One way to enable this is to extract accurate derivative or sensitivity information from such EM-based modeling techniques and supply the numerical derivatives to CAD algorithms. In addition, the proposed EM-based modeling techniques when combined with evolutionary design methods, *e.g.* genetic algorithms, could lead to even more efficient RF and microwave design and optimization.

5.2 Future Work

EM-based modeling techniques which account for high-order EM effects represents one of the most recent trends in RF and microwave computer aided design. Such techniques, including those presented in this thesis aim to achieve highest level of speed, precision and automation, in an attempt to meet the challenges posed by the next generation of high frequency design. These techniques are combined with state-of-the-art CAD technologies creating numerous opportunities for industrial applications at various stages of high frequency CAD including modeling, simulation and design.

The new dynamic grid concept possesses a unique quality which makes it attractive. This concept is "generic" in the sense that it can be applied to other modeling methods such as ANN to further reduce the number of training data. Once the dy-

namic grid is integrated with other numerical modeling techniques *e.g.* ANN, it is important that we continue to incorporate such concepts as they evolve into readily usable tools. A key requirement is to develop plug-in software tools that can be embedded into currently available EM simulator environments for carrying out circuit- and system-level CAD.

The space mapping based temperature modeling technique has already led to robust designs in industry. However this technique can be modified and extended for other structures as well as higher order filter designs with several combline resonators. The in-house implemented technique can also be turned to a user-friendly tool available to RF/microwave designers.

Finally, the application of FDTD-based technique in temperature modeling of combline resonators is confirmed to be accurate. The future work includes incorporation of FDTD-based technique with evolutionary design methods such as genetic algorithms. Such evolutionary algorithms are capable of handling optimization problems with numerous goals and constraints including technical user specifications and feasibility of designs implementation. Such algorithms have tremendous potential for designing combline resonators which their frequency response is intrinsically independent of temperature.

References

[1] J.E. Dennis, Jr., and J.J. Moré, "Quasi-Newton methods, motivation and theory," *SIAM Rev.*, vol. 19, pp. 46-89, 1977.

[2] D. Le, "A fast and robust unconstrained optimization method requiring minimum storage," *Math. Program*, vol. 32, pp. 41-68, 1985.

[3] em^{TM}, Sonnet Software, Inc., 1020 Seventh North Street, Suite 210, Liverpool, NY 13088.

[4] *Maxwell Eminence*^{TM}, Version 4.02, Ansoft Corporation, Four Station Square, Suite 660, Pittsburgh, PA 15219, USA.

[5] V. Rizzoli, A. Costanzo, C. Cecchetti, and D. Masotti, "Computer-aided optimization of broadband nonlinear microwave integrated circuits with the aid of electro- magnetically generated look-up tables," *Microwave Opt. Tech. Letter*, vol. 15, pp. 189-196 , 1997.

[6] J. F. Liang and K. A. Zaki, "CAD of microwave junctions by polynomial curve fitting," *IEEE Trans. Microwave Theory Tech.*, vol. 1, pp. 451-454 , 1993.

[7] J.W. Bandler, Q.S. Cheng, D.M. Hailu, and N.K. Nikolova, "A space-mapping design framework," *IEEE Trans. Microwave Theory Tech.*, vol. 52, pp. 2601-2610, 2004.

[8] Q. J. Zhang and K. C. Gupta, *Neural Networks for RF and Microwave Design*, Norwood, MA: Artech House, 2000.

[9] A.H. Zaabab, Q-J. Zhang, and M. Nakhla, "A neural network modeling approach to circuit optimization and statistical design," *IEEE Trans. Microwave Theory Tech.*, vol. 43, pp. 1349-1358, 1995.

[10] Q.J. Zhang, K.C. Gupta, and V.K. Devabhaktuni, "Artificial neural networks for RF and microwave design - From theory to practice," *IEEE Trans. Microwave Theory Tech.*, vol. 51, pp. 1339-1350, 2003.

[11] F. Wang, V.K. Devabhaktuni, C. Xi, and Q.J. Zhang, "Neural network structures and training algorithms for RF and microwave applications," *Int. J. RF Microwave CAE*, vol. 9, pp. 216-240, 1999.

[12] M.H. Bakr, J.W. Bandler, R.M. Biernacki, S.H. Chen, and K. Madsen, "A trust region aggressive space mapping algorithm for EM optimization," *IEEE Trans. Microwave Theory Tech.*, vol. 46, pp. 2412-2425, 1998.

[13] E.K. Miller, "Solving bigger problems - By decreasing the operation count and increasing the computation bandwidth," *Proc. IEEE*, vol. 79, pp. 1493-1504, 1991.

[14] D.D. Zutter, J. Sercu, T. Dhaene, J.D. Geest, F.J. Demuynck, S. Hammadi, and C.W.P. Huang, "Recent trends in the integration of circuit optimization and full-wave electromagnetic analysis," *IEEE Trans. Microwave Theory Tech.*, vol. 52, pp. 245-256, 2004.

[15] R. Lehmensiek and P. Meyer, "Creating accurate multivariate rational interpolation models of microwave circuits by using efficient adaptive sampling to minimize the number of computational electromagnetic analyses," *IEEE Trans. Microwave Theory Tech.*, vol. 49, pp. 1419-1430, 2001.

[16] A. Kashi and V.K. Devabhaktuni, "Enhanced adaptive frequency sampling for RF and microwave CAD," *Proc. EuMC*, Manchester, UK, pp. 470-473, Sept. 2006.

[17] U. Beyer and F. Smieja, "Data exploration with reflective adaptive models," *Comp. Stat. Data Anal.*, vol. 22, pp. 193-211, 1996.

[18] V.K. Devabhaktuni, M.C.E. Yagoub, and Q.J. Zhang, "A robust algorithm for automatic development of neural-network models for microwave applications," *IEEE Trans. Microwave Theory Tech.*, vol. 49, pp. 2282-2291, 2001.

[19] S.F. Peik, R.R. Mansour, and Y.L. Chow, "Multidimensional Cauchy method and adaptive sampling for an accurate microwave circuit modeling," *IEEE Trans. Microwave Theory Tech.*, vol. 46, pp. 2364-2371, 1998.

[20] M. Mattes and J.R. Mosig, "A novel adaptive sampling algorithm based on the survival-of-the-fittest principal of genetic algorithms," *IEEE Trans. Microwave Theory Tech.*, vol. 52, pp. 265-275, 2004.

[21] K. Kottapalli, T.K. Sarkar, Y. Hua, E.K. Miller, and G.J. Burke, "Accurate computation of wide-band response of electromagnetic systems utilizing narrow-band information," *IEEE Trans. Microwave Theory Tech.*, vol. 39, pp. 682-687, 1991.

[22] R.S. Adve and T.K. Sarkar, "Generation of accurate broadband information from narrowband data using the Cauchy method," *Microwave Opt. Technol. Lett.*, vol. 6, pp. 569-573, 1993.

[23] J. Ureel, N. Fach, D.D. Zutter, and P. Lagasse, "Adaptive frequency sampling of scattering parameters obtained by electromagnetic simulation," *Proc. IEEE AP-S Int. Symp.*, Seattle, WA, pp. 1162-1165, June 1994.

[24] T. Dhaene, J. Ureel, N. Fach, and D.D. Zutter, "Adaptive frequency sampling algorithm for fast and accurate S-parameter modeling of general planar structures," *Proc. IEEE MTT-S Int. Microwave Symp.*, Orlando, FL, pp. 1427-1430, May 1995.

[25] R.S. Adve, T.K. Sarkar, S.M. Rao, E.K. Miller, and D.R. Pflug, "Application of the Cauchy method for extrapolating/interpolating narrow-band system responses," *IEEE Trans. Microwave Theory Tech.*, vol. 45, pp. 837-845, 1997.

[26] J.D. Geest, T. Dhaene, N. Fach, and D.D. Zutter, "Adaptive CAD-model building algorithm for general planar microwave structures," *IEEE Trans. Microwave Theory Tech.*, vol. 47, pp. 1801-1809, 1999.

[27] J. Stoer and R. Bulirsch, Introduction to Numerical Analysis. Berlin, Germany: Springer-Verlag, 1980.

[28] A. Cuyt, R. B. Lenin, S. Becuwe, and B. Verdonk, "Adaptive multivariable rational data fitting with application in electromagnetics," *IEEE Trans. Microwave Theory Tech.*,vol. 54, pp. 2265-2274, 2006.

[29] I. Gohberg, T. Kailath, and V. Olshevsky, "Fast Gaussian elimination with partial pivoting for matrices with displacement structure," *Math. Comput.*, vol. 64, no. 212, pp. 1557-1576, 1995.

[30] T. Kailath and V. Olshevsky, "Displacement ranks of a matrix," Bull. Amer. Math. Soc. (N.S.), vol. 1, no. 5, pp.769-773, 1979.

[31] T. Kailath , "Displacement ranks of matrices and linear equations," J. Math. Anal. Appl., vol. 68, no.2, pp. 395-407, 1979.

[32] I. Schur, "Uber potenzreeihen die im Inneren des Einheitskreises beschrankt sind," *Jounal fur die Reine und Angewandte Mathematik*, 147 (1917), pp. 205 - 232. English translation : in Operator Theory : Advances and Applications (I.Gohberg. ed.), vol. 18, pp. 31-88, Birkhauser, Boston, 1986.

[33] H. Lev-Ari and T. Kailath, "Triangular factorization of structured Hermitian matrices," *Operator Theory: Advances and Applications*, 18 (19986), pp. 301-324, (I.Gohberg, ed.), Birkhauser, Boston.

[34] R. Pintelon and J. Schoukens, *System Identification: A Frequency Domain Approach.* Piscataway, NJ: IEEE Press, 2001.

[35] Q.S. Cheng and J.W. Bandler, "An implicit space mapping technique for component modeling," *Proc. EuMC*, Manchester, UK, Sept. 2006, pp. 459-461.

[36] C. Wang and K.A. Zaki, "Temperature compensation of combline resonators and filters," *IEEE MTT-S Int. Microwave Symp. Dig.*, Anaheim, CA, June 1999, pp. 1041-1044.

[37] B.F. Keats, R.B. Gorbet, and R.R. Mansour, "Design and testing of SMA temperature-compensated cavity resonator," *IEEE Trans. Microwave Theory Tech.*, vol. 51, pp. 2284-2289, 2003.

[38] P. Martin, "The temperature sensitivity of coaxial and slabline resonators," *Proc. Asia-Pacific Microwave Conference*, Sydney, Australia, Dec. 2000, pp. 495-498.

[39] A. Kashi, P. Kumar, M. Caron, and Vijay K. Devabhaktuni, "A Space-Mapping Based CAD Methodology for Modeling Temperature Characteristics of Combline Resonators," *PIERS Proceedings*, Beijing, China, March 2007, pp. 1980-1984.

[40] B.F. Nicholson, "The resonant frequency of interdigital filter elements", *IEEE Trans. Microwave Theory Tech.*, vol.14, pp. 250-251, 1966.

[41] P.I. Solmo, "The computation of coaxial line step capacitances", *IEEE Trans. Microwave Theory Tech.*, vol. 15, pp. 48-53, 1967.

[42] J.W. Bandler, Q. Cheng, S.A. Dakroury, A.S. Mohamed, M.H. Bakr, K. Madsen and J. Sndergaard, "Space mapping: the state of the art," *IEEE Trans. Microwave Theory Tech.*, vol. 52, no. 1, pp. 337-361, 2004.

[43] M. Pozar, *Microwave Engineering*, New York, NY: John Wiley & Sons, 2000.

[44] S. Dey, R. Mittra, "Efficient computation of resonant frequencies and quality factors of cavities via a combination of the finite-difference time-domain technique and the Padé approximation," *Microwave Guided Wave Lett.*, vol. 8, pp. 415-417, 1998.

[45] S. Groiss, I. Bardi, O. Biro, K. Preis, and K. R. Richter, "Parameters of lossy cavity resonators calculated by the finite element method," *IEEE Trans. Magn.*, vol. 32, pp. 1246-1249, 1996.

[46] Yinchao, R. Mittra, P. Harms, "Finite-difference time-domain algorithm for solving Maxwell's equations in rotationally symmetric geometries," *IEEE Trans. Microwave Theory Tech.*, vol. 44, pp. 832-839, 1996.

[47] K. S. Yee, "Numerical solution of initial boundary value problems involving Maxwell's equations in isotropic media," *IEEE Trans. Antenna Propagat.*, vol. AP-14, pp. 302-307, 1966.

[48] Y. Chen, K. Sun, B. Beker, and R. Mittra, "Unified matrix representation of Maxwell's and wave equations using generalized differential matrix operators," *IEEE Trans. Education*, vol. 41, pp. 61-68, 1998.

[49] F. J. Harris, "On the use of windows for harmonic analysis with discrete Fourier transform," *Proceedings of the IEEE*, vol. 66, pp. 51-83, 1978.

[50] A. Bondeson, T. Rylander, P. Ingelstrom, *Computational Electromagnetics*, New York, NY: Springer, 2005.